Cloud Detection in Nonpolar Regions for CERES Using TRMM VIRS and Terra and Aqua MODIS Data

Patrick Minnis, Qing Z. Trepte, Szedung Sun-Mack, Yan Chen, David R. Doelling, David F. Young,
Douglas A. Spangenberg, Walter F. Miller, Bruce A. Wielicki, Ricky R. Brown,
Sharon C. Gibson, and Erika B. Geier

Abstract—**Objective techniques have been developed to consistently identify cloudy pixels over nonpolar regions in multispectral imager data coincident with measurements taken by the Clouds and Earth's Radiant Energy System (CERES) on the Tropical Rainfall Measuring Mission (TRMM), Terra, and Aqua satellites. The daytime method uses the 0.65-, 3.8-, 10.8-, and 12.0-μm channels on the TRMM Visible and Infrared Scanner (VIRS) and the Terra and Aqua MODIS. The VIRS and Terra 1.6-μm channel and the Aqua 1.38- and 2.1-μm channels are used secondarily. The primary nighttime radiances are from the 3.8-, 10.8-, and 12.0-μm channels. Significant differences were found between the VIRS and Terra 1.6-μm and the Terra and Aqua 3.8-μm channels' calibrations. Cascading threshold tests provide clear or cloudy classifications that are qualified according to confidence levels or other conditions, such as sunglint, that affect the classification. The initial infrared threshold test classifies ∼43% of the pixels as clouds. The next level seeks consistency in three (two) different channels during daytime (nighttime) and accounts for roughly 40% (25%) of the pixels. The third tier uses refined thresholds to classify remaining pixels. For cloudy pixels, ∼4% yield no retrieval when analyzed with a cloud retrieval algorithm. The techniques were applied to data between 1998 and 2006 to yield average nonpolar cloud amounts of ∼0.60. Averages among the platforms differ by < 0.01 and are comparable to surface climatological values, but roughly 0.07 less than means from two other satellite analyses, primarily as a result of missing small subpixel and thin clouds.**

Index Terms—**Cloud, cloud detection, cloud mask, Clouds and Earth's Radiant Energy System (CERES), Moderate Resolution Imaging Spectroradiometer (MODIS), Visible and Infrared Scanner (VIRS).**

I. INTRODUCTION

SIMULTANEOUS measurement of the radiation and cloud fields on a global basis has long been recognized as a key component in understanding and modeling the interaction between clouds and radiation at the top of the atmosphere, at the surface, and within the atmosphere. The NASA Clouds and Earth's Radiant Energy System (CERES) Project [1] began meeting this need in 1998 with the launch of its first broadband shortwave and total band scanners along with the Visible and Infrared Scanner (VIRS) on the Tropical Rainfall Measuring Mission (TRMM) satellite in late 1997. During late 1999 and early 2002, the Terra and Aqua satellites, respectively, were launched with instrument packages that included two CERES scanners each and the Moderate Resolution Imaging Spectroradiometer (MODIS). Together, those satellites have been providing the most comprehensive global characterization of clouds and radiation to date. CERES was designed to fly with high-resolution imagers so that the cloud conditions could be evaluated for every CERES measurement. The cloud properties, specifically, cloud fraction, phase, temperature, height, optical depth, effective particle size, and condensed/frozen water path, are key parameters needed to link the atmospheric radiation and hydrological budgets. Among other applications, they are essential for selecting the proper anisotropic directional models [2] used to convert the CERES radiances to the shortwave albedo and the longwave fluxes needed to define the radiation budget (ERB) at the top of the atmosphere (TOA). Cloud and aerosol properties coincident with broadband radiation measurements are also necessary for sorting out the direct and indirect effects of aerosols on climate. In summary, the combined data sets are critical to understanding the impact of clouds on the ERB at the surface and on the radiative heating profile within the atmosphere. By combining the broadband fluxes with cloud and aerosol properties determined in a radiatively consistent manner, the CERES data set should provide an unprecedented set of constraints for climate model assessment and improvement.

The CERES program planned, from its inception [3], [4], to analyze coincident imager data to obtain cloud and aerosol properties that could be precisely matched with the CERES scanner fields of view. To obtain a data set useful for studying climate trends, it was recognized that the above cloud and radiation fields must be determined using consistent algorithms, auxiliary input (e.g., atmospheric temperature and humidity profiles), and calibrations across platforms to minimize instrument- and algorithm-induced changes in the record. By combining the precessing orbit TRMM data with the late

morning Terra and early afternoon Aqua observations, CERES would measure the complete diurnal cycle of clouds and radiation for the Tropics and obtain unprecedented sampling of those same fields in the extra-tropics. Because of the requirements for consistency, simultaneity, and collocation between the cloud and radiation measurements, it was necessary to develop a set of algorithms and a processing system independently of other global cloud processing systems that were either operating or being developed prior to launch of the first CERES-bearing orbiter. The International Satellite Cloud Climatology Project (ISCCP) has been deriving cloud properties from geostationary and NOAA polar-orbiting satellites since 1983 [5], but its products could not be used because ISCCP samples the imager data at an effective resolution of $\sim$32 km (larger than a CERES footprint, $\sim$20 km), cloud particle size is assumed in the retrievals, and simultaneity with the CERES satellites is very limited. The MODIS Atmosphere Science Team (MAST) also planned to derive pixel-level cloud properties from the MODIS data [6], [7] but employed algorithms that used many of the 36 MODIS spectral bands and auxiliary input data that are not necessarily consistent over time. The MAST algorithms, which have been used to generate the MOD06 and MOD35 products [8], precluded the use of the VIRS because it is limited to five channels and would not be able to yield cloud properties consistent with the MOD06 and MOD35 results. Furthermore, CERES requires complete cloud information for each footprint, and that is not always available in the MOD06 products.

Although the failure of the TRMM CERES scanner early in the mission obviated some of the consistency requirements, other more important factors necessitated the development of independent cloud and aerosol analysis algorithms. CERES is an end-to-end processing system with cloud properties feeding into subsystems that determine TOA, surface, and atmospheric radiative fluxes, including a complex time-space averaging subsystem that employs geostationary satellite measurements [1]. The cloud detection and retrieval algorithms had to be responsive to the needs of the downstream processing systems and had to be as consistent as possible with the CERES geostationary satellite data processing system [9]. Given the limitations of external cloud data sets and the internal team interaction and consistency requirements, a unique set of cloud detection and retrieval algorithms was developed for CERES utilizing as few channels as possible while producing stable and accurate cloud properties that are compatible with the CERES anisotropic models.

The first step in the cloud retrievals is discriminating between cloudy and cloud-free pixels, the cloud mask. Methods for distinguishing between cloudy and clear pixels are as many and diverse as the motivations for using them, as discussed in detail by Gomez-Chova *et al.* [10]. Generally, each technique is developed to accomplish a certain goal that involves treating clouds as interference or as information. For example, the ISCCP was designed to provide a long-term cloud climatology that covers the diurnal cycle. Thus, it used only 0.65- and 11-μm channels on geostationary satellites to ensure the ability to perform consistent analyses over many years, even though more spectral channels have become available during the last decade. To minimize cloud contamination in their aerosol retrievals, the MAST aerosol group developed a cloud mask [11] based on spatial variability that differs from that used by the MAST clouds group [6]. Monitoring ocean color also seeks to minimize cloud interference but uses spectral ratios to determine cloud-free scenes [12]. The motivation for developing the CERES mask was designed for consistency over time among different satellite instruments with the primary goal of accurately detecting those clouds having the greatest radiative impact on the radiation budget.

This paper provides an overview of the algorithms used by CERES to detect clouds in nonpolar regions. The CERES cloud mask defines a given imager pixel as clear or cloudy or, in some cases, as bad data. The clear and cloudy classifications are further denoted as weak or good to denote a level of certainty, the former being less certain than the latter. The weak category is defined based on how close the observed radiances come to the expected clear-sky values. In clear conditions, the pixel can also be identified as being covered by aerosol (e.g., heavy dust), smoke, fire, shadow, or snow, or affected by sunglint. Cloudy pixels can also be identified as being affected by sunglint. The subclassifications are made available to users in deciding whether the results are reliable and whether they can be useful for studying certain phenomena such as aerosol radiative forcing or snow albedo.

This is the first of a series of four papers [13]–[15] that describe the CERES cloud analysis system for VIRS Edition 2 (Ed2), Terra Ed2, and Aqua Edition 1 (Ed1). The initial VIRS cloud mask was completed in 1998 and updated, along with Terra Ed1, to the Ed2 versions in 2003. Processing of the MODIS data for CERES using all three of the editions described here began during 2004.

II. DATA

The input data used in the CERES cloud detection algorithms consist of the imager radiances and fixed and variable ancillary information.

A. Satellite Radiances

1) VIRS: The TRMM VIRS is a five-channel imager that measures radiances at 0.65 (visible, VIS), 1.61 (near-infrared, NIR), 3.78 (shortwave-infrared, SIR), 10.8 (infrared, IR), and 12.0 (split window, SW) μm with a nominal 2-km spatial resolution [16]. Table I lists the VIRS and MODIS channels available to CERES. For simplicity, unless otherwise noted, the CERES reference channel numbers will be used throughout this paper to refer to a given wavelength. The VIRS cross-track scan extends out to a viewing zenith angle VZA (θ) of 48° and, from the 35° inclined orbit, yields coverage roughly between 38° N and 38° S. The TRMM orbit gives the VIRS a viewing perspective distinctly different from either geostationary or Sun-synchronous satellites. It samples all local times of day over a 45-day period. At the Equator, this sampling is evenly distributed over the period, but, at higher latitudes, the views are primarily in darkness for roughly two weeks followed by two weeks of sunlight. The CERES shortwave and total broadband

TABLE I
IMAGER CHANNELS INGESTED IN CERES PROCESSING AND USED IN
CERES CLOUD MASK. VIRS DATA ARE 2-km RESOLUTION. ALL
MODIS DATA ARE 1-km RESOLUTION, EXCEPT FOR CHANNEL 1,
WHICH HAS BOTH 1- AND 0.25-km RESOLUTIONS

CERES Reference Channel #	VIRS Channel #	Central Wavelength (μm)	MODIS Channel #	Central Wavelength (μm)	Use
1	1	0.620	1	0.645	All
2	2	1.610	6	1.640	1,2,3
3	3	3.780	20	3.792	All
4	4	10.83	31	11.030	All
5	5	12.01	32	12.020	All
6			29	8.550	2,3,4,5
7			7	2.130	4,5
8			26	1.375	4
9			27	6.720	3,5
10			2	0.858	
11			3	0.469	
12			4	0.555	
13			5	1.240	
14			17	0.905	
15			23	4.050	
16			33	13.34	
17			34	13.64	
18			35	13.94	
19			36	14.24	

Use Key:
1 - VIRS Edition2
2 - *Terra* Edition 2 Nonpolar
3 - *Terra* Edition 2 Polar
4 - *Aqua* Edition 1 Nonpolar
5 - *Aqua* Edition 1 Polar

scanners have a nominal field of view size of ∼10 km. The VIRS data were obtained from the NASA Langley Distributed Active Archive Center.

Version-5a VIRS data are analyzed by CERES at full resolution. The Version-5a VIRS VIS SIR, IR, and SW channel calibrations appear to be quite stable [17]–[19], but there is a slight day–night calibration difference in the IR and SW channels that is not taken into account here [18]. The VIRS NIR channel suffers from a thermal leak at 5.2 μm that is corrected using an updated version [20] of the Ignatov and Stowe correction [21]. Although no other calibration problems were revealed in initial studies [22], [23], they did not examine the absolute calibration of the channel. Other investigations of the VIRS NIR channel indicated that its gain was too low by ∼0.17 compared to other data and theoretical computations using cloud microphysical models [17], [24].

The MODIS and VIRS 1.6-μm channels have similar spectral bands and, therefore, should produce similar reflectances for the same scene. To further investigate the apparent 17% calibration discrepancy, the Terra MODIS and VIRS NIR channel radiances were matched and intercalibrated as in [19] using data taken over ocean from every other month between March 2000 and March 2004 when Version 5a ended. Fig. 1 shows scatter plots with linear regressions for matched data from two of those months. The VIRS radiances were normalized to the MODIS solar constant of 75.05 $W \cdot m^{-2} \cdot sr^{-1} \cdot \mu m^{-1}$. The slopes of the fits are 1.209 and 1.177 for March and September 2001, respectively. Overall, the slopes ranged from 1.163 in November 2003 to 1.232 with a mean value of 1.193, and the mean offset was 0.0 $W \cdot m^{-2} \cdot sr^{-1} \cdot \mu m^{-1}$. No significant trends were detected during the four-year period. A small portion of the differences in the gains may be due to the slight differences in the spectral response functions, but the majority of the discrepancy is due to underestimation of the radiances by the VIRS calibration. The 1.17 correction factor applied to the VIRS NIR channel during the CERES processing should

have taken care of much of the calibration bias. Although the TRMM CERES scanner failed after August 1998 and was resuscitated for 1 month, March 2000, the TRMM Ed2 CERES cloud products were also generated from VIRS data taken from January 1998 to July 2001. VIRS continues to operate as of this writing.

2) MODIS: Terra MODIS [25] began collecting data starting in late February 2000 from a Sun-synchronous orbit with a 1030-LT equatorial crossing time. Aqua MODIS became operational in July 2002 from a Sun-synchronous orbit with a 1330-LT equatorial crossing time. CERES ingests a 19-channel subset of the 36-channel MODIS complement (Table I) with the intention of using additional channels in future editions of the algorithms and in other subsystems besides the cloud codes. The 0.25-km channel-1 (0.645 μm) pixels corresponding to the 1-km channel-1 pixels are also included in the ingested data for future use. The 1-km MODIS data are sampled every other pixel and every other scan line to reduce processing time. This subsetted data set, provided by the NASA Goddard Space Flight Center Distributed Active Archive Center, was further reduced by sampling every other pixel during actual processing, yielding an effective resolution of 8 km. For a given CERES footprint (∼20 km at nadir for Aqua and Terra), the subsampling yields unbiased cloud amounts relative to the full resolution sampling. The standard deviation of the cloud amount differences between the full and subsampled data set is 0.035. The CERES-MODIS (CM) Terra Ed2 cloud analysis algorithms use the 0.65-, 1.64-, 3.79-, 10.8-, and 12.0-μm channels. Because the Aqua 1.64-μm channel did not operate properly, the Aqua Ed1 nonpolar cloud mask used the 2.13-μm channel (CERES reference channel 7) instead. In addition, the Aqua Ed1 algorithms used the 1.38- and 8.5-μm channels to improve thin cirrus cloud detection after some obvious deficiencies were found in the Terra Ed2 cloud mask.

The Terra VIS channel gain was found to drop by 1.17% after November 18, 2003, but otherwise had no trends. That sudden calibration change is not taken into account in Terra Ed2 nor has it disappeared in Terra MODIS Collection-5 data. If that decrease is taken into account for all Terra data taken after a noted date, the trend-free Aqua VIS channel gain is 1% greater than its Terra counterparts [19]. The Aqua reflectance is 4.6% greater, on average, than that from VIRS, a result that is consistent with the theoretical differences between the VIRS and MODIS spectral windows. The gain in the Terra 1.64-μm channel was examined for trends using the deep convective cloud method as in [19]. A statistically insignificant decrease in the gain of 0.27% y^{-1} was found from linear regression. It is concluded that the Terra 1.64-μm channel calibration is stable during the six-year period.

The relative calibrations of the Aqua and Terra 3.79-, 10.8-, and 12.0-μm channels were examined using the methods of Minnis *et al.* [18], [19]. Fig. 2 shows scatter plots of the matched 3.79-μm data taken over the polar regions on August 2004. During daytime [Fig. 2(a)], the slope of the linear fit is 1.006, and on average, the Terra SIR brightness temperatures are 0.57 K greater than those from Aqua. This result is typical for the period between 2002 and 2006 (Table II), during which the mean difference is 0.55 K with no trends. At night,
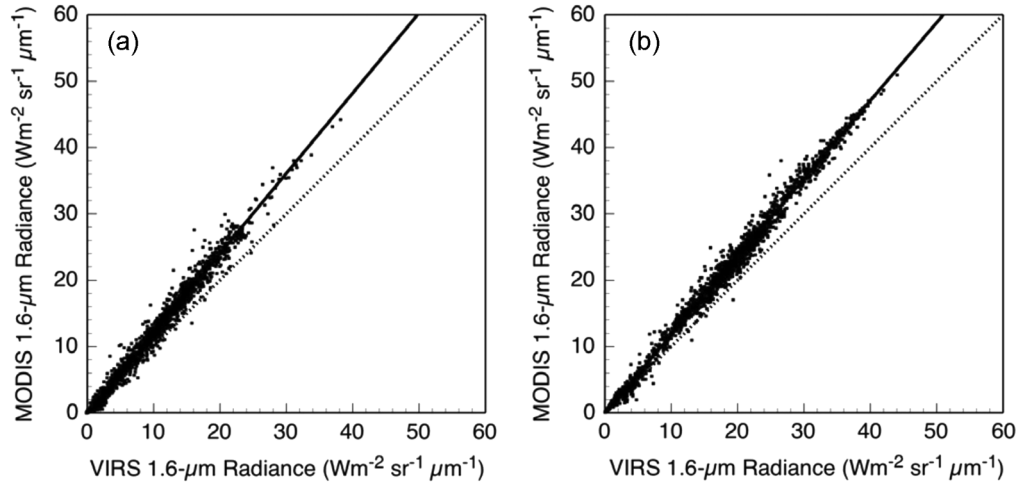
Fig. 1.   Intercalibration of VIRS channel-2 and Terra MODIS channel-6 radiances over ocean for (a) March and (b) September 2001.
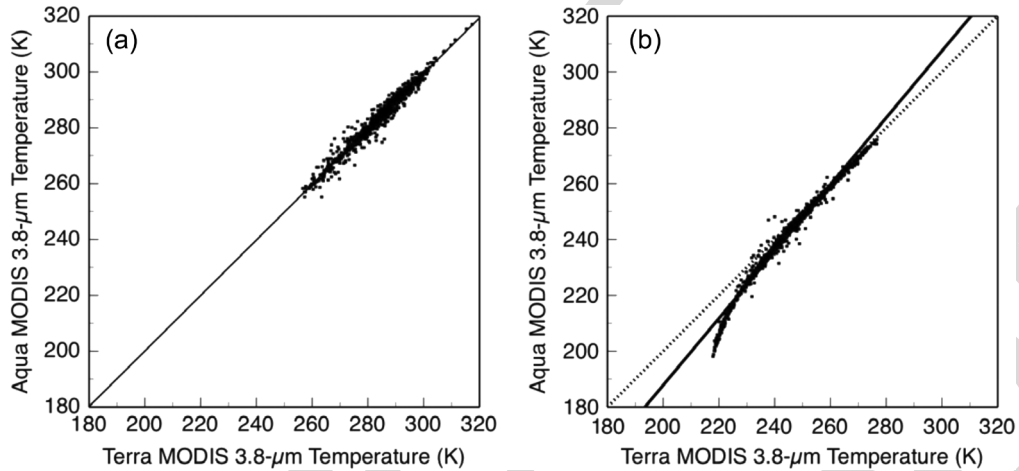

Fig. 2.   Intercalibration of Aqua and Terra MODIS channel-20 brightness temperatures on August 2004 during the (a) day and (b) night.

data having brightness temperatures $T_b > 250$ K are linearly correlated as during the daytime, but the Terra temperatures asymptote to a value of 218 K as the Aqua values reach 197 K. This behavior is seen in every month of the intercalibrations indicating a systematic problem with the Terra data at night. In the initial VIRS-Terra intercalibrations [18], there were too few data points to definitively determine this discrepancy at the low end of the Terra temperature range. Thus, the VIRS-Terra intercalibrations were repeated for the 2002–2006 period using data from every other month. The nocturnal results are the same as those in Fig. 2(b). The large biases in the average SIR brightness temperature differences (BTDs) at night for Terra and Aqua (Table II) reflect the strong contribution of the colder temperatures to the average because the data were taken over polar regions, whereas less conspicuous nighttime BTDs for VIRS-Terra and VIRS-Aqua result from having fewer very low temperatures during the tropical night. During the day, the VIRS SIR brightness temperatures are 1.39 K and 0.85 K less than the Terra and Aqua values, respectively, confirming the 0.55-K bias between Aqua and Terra SIR daytime data.

The intercalibrations among the three instruments' IR and SW channels are summarized in Table II. The differences between the Terra and Aqua 10.8- and 12.0-μm T_b's are slightly

TABLE II
AVERAGE DIFFERENCES IN MATCHED BRIGHTNESS TEMPERATURES
FROM THERMAL CHANNEL INTERCALIBRATIONS

Satellite Pair	3.8 μm (K)		10.8 μm (K)		12.0 μm (K)	
	Day	Night	Day	Night	Day	Night
VIRS-*Aqua*	-0.85	-0.35	0.26	-0.08	-0.94	-0.83
VIRS-*Terra*	-1.39	-1.01	0.21	-0.06	-1.00	-0.88
Terra - Aqua	0.55	2.29	0.01	0.16	0.04	0.16

larger at night than during the daytime. This difference appears to be the result of somewhat larger Terra T_b's at the low end of the range, temperatures that are infrequently observed in the daytime comparisons. This discrepancy at the low end appears to have been eliminated in the MODIS Collection-5 data. Roughly half of the nearly 1-K bias between the VIRS and MODIS SW T_b's can be explained by the differences in the spectral response functions [18]. In the data processing, spectral differences are taken into account theoretically. The only calibration corrections made to the raw radiances are those for the VIRS 1.6-μm channel, as noted earlier. The other calibration differences, such as those in Fig. 2 and discussed earlier, were not corrected prior to analysis because they were not known before the start of the subject CERES Edition

processing. To date, the CERES cloud analysis algorithms have been applied to Terra and Aqua Collection-4 MODIS data through April 2006 and to Collection-5 MODIS data from January to December 2006.

B. Variable Ancillary Data

The CERES Meteorology, Ozone, and Aerosol (MOA) data set includes vertical profiles of temperature, humidity, wind, and ozone and total aerosol amounts. The ozone data, which include the total column concentration, are taken from the 2.5° National Centers for Environmental Prediction's Stratosphere Monitoring Ozone Blended Analysis (SMOBA) [26] or from the Earth Probe Total Ozone Mapping Spectrometer (total column optical depth only) at a 1.25° resolution when SMOBA data are not available. The CERES MOA temperature, wind, and humidity profiles are based on numerical weather analyses (NWAs): The European Centre for Medium-range Weather Forecasting (ECMWF) reanalyses for VIRS and on the Global Modeling Assimilation Office GEOS 4.03 analyses [27] for the MODIS processing. The ECMWF profiles were available at a nominal resolution of 0.5° every 6 h, and surface skin temperature T_{skin} was available every 3 h. GEOS profiles and skin temperatures were made available at the same temporal resolutions on a 1° grid. All input MOA data were interpolated to produce, ~~on a common~~ $1° \times 1°$ ~~grid~~, surface skin temperature, geopotential height, pressure, total column ozone, profiles of temperature, specific humidity, and ozone at up to 58 levels from the surface to 0.1 hPa [28].

Daily ice and snow extent data were obtained from the Near Real-Time SSM/I EASE-Grid Daily Global Ice Concentration and Snow Extent products [29] on a nominal 25-km polar stereographic grid and supplemented by the NESDIS Interactive Multisensor Snow and Ice Mapping System Daily Northern Hemisphere Snow and Ice Analysis in the vicinity of coastlines [30]. All snow and ice extent values were interpolated to a 10' grid.

For land and snow surfaces, monthly updated VIS overhead-sun clear-sky albedos

$$\alpha_{\text{cso1}}(\lambda, \phi) = \alpha_{\text{cs1}}(\lambda, \phi; \mu_o = 1) \tag{1}$$

were derived on a 10' grid from VIRS and MODIS 0.64-μm data along with overhead-sun NIR surface albedos $\alpha_{\text{si}}(\lambda, \phi; \mu_o = 1)$ for channels 2 and 7 from VIRS and Terra MODIS 1.64-μm data and from the MODIS 2.13-μm data using clear-sky values from earlier versions of the CERES processing system [15], [31], [32]. The latitude and longitude are indicated by λ and ϕ, respectively, whereas $\mu_o = \cos(\text{SZA})$ and SZA is the solar zenith angle. These albedos are used with angular directional models and, for the NIR channels, with approximations for atmospheric absorption to estimate the clear-sky reflectance for a given scene. From the overhead-sun albedos, the VIS clear-sky albedo is estimated at a given SZA for any 10' region as

$$\alpha_{\text{cs1}}(\lambda, \phi; \mu_o) = \delta_{\text{cs1}}(K(\lambda, \phi); \mu_o) \alpha_{\text{cso1}}(\lambda, \phi) \tag{2}$$

where δ_{cs1} is a normalized directional reflectance model that predicts the variation of the clear-sky albedo with SZA for a given surface type K, which is one of the 19 modified International Geosphere Biosphere Program (IGBP) surface types [33]. Similarly, the NIR surface albedo at a given SZA for any 10' region is estimated as

$$\alpha_{\text{si}}(\lambda, \phi; \mu_o) = \delta_{\text{si}}(K(\lambda, \phi); \mu_o) \alpha_{\text{soi}}(\lambda, \phi) \tag{3}$$

where i indicates either channels 2 or 7 and the subscript o denotes overhead sun conditions. Values of the directional reflectance models and their derivation can be found in Sun-Mack *et al.* [15], [31] for all surfaces except snow and water, where the updated model of Minnis and Harrison [34] is employed.

The VIS clear-sky reflectance is estimated as

$$\rho_{\text{cs1}}(\lambda, \phi; \mu_o, \mu, \psi) = \alpha_{\text{cs1}} \chi_{\text{VIS}}(K; \mu_o, \mu, \psi) \tag{4}$$

where χ_{VIS} is the VIS bidirectional reflectance distribution function (BRDF), $\mu = \cos(\text{VZA})$, and ψ is the relative azimuth angle. For the NIR channels 2 and 7, the predicted clear-sky reflectance is

$$\rho_{\text{csi}} = \alpha_{\text{si}} \chi_{\text{si}}(K; \mu_o, \mu, \psi) t_i \tag{5}$$

where χ_{si} is the NIR BRDF and t_i is the combined transmittance of the atmosphere to the downwelling and upwelling beam for channel i [31]. The VIS BRDFs are taken from Minnis and Harrison [34] for water surfaces ($K = 17$) and from Suttles *et al.* [35] for land and coast ($K = 1 - 14, 18, 19$), snow ($K = 15$), and desert ($K = 16$). The theoretical snow BRDF described by Sun-Mack *et al.* [31] is employed for the MODIS analyses. The VIS BRDF model of Minnis and Harrison [34] was also used for the NIR channels over water surfaces. BRDFs from Kriebel [36] were used for the NIR channels over most land surfaces as described in [31], whereas the broadband desert model of Suttles *et al.* [35] was used for the NIR for deserts and the theoretical models described in [31] were used for snow and ice surfaces.

Uncertainties were computed from the same database used to determine the clear-sky and surface albedos [31]. Nominally, the relative rms average $\sigma_{\text{cs1}}(\lambda, \phi, m)$ of the temporal and spatial standard deviations of the mean $\langle \alpha_{\text{cso1}}(\lambda, \phi, m) \rangle$ of $\alpha_{\text{cso1}}(\lambda, \phi)$ were computed for each month m using daily pixel-level data from the earlier editions of the VIRS and Terra MODIS analyses. These values were normalized to $\langle \alpha_{\text{cso1}}(\lambda, \phi, m) \rangle$ to obtain the basic uncertainty in the monthly mean overhead sun albedos. The resulting uncertainties were filtered to eliminate values from poorly sampled areas where mostly cloudy conditions prevailed during the month. The filtered data were then averaged for each surface type to obtain $\langle \alpha_{\text{cso1}}(K, m) \rangle$ and $\sigma_{\text{cs1}}(K, m)$. These surface-type averages were then used to fill in uncertainty values for each region of the given surface type that had no results for the month. When the final edition processing took place, these uncertainties were replaced with default values whenever the nominal value was less than the default value. A similar process was used for channels 2 and 7. It is recognized that, although high-resolution
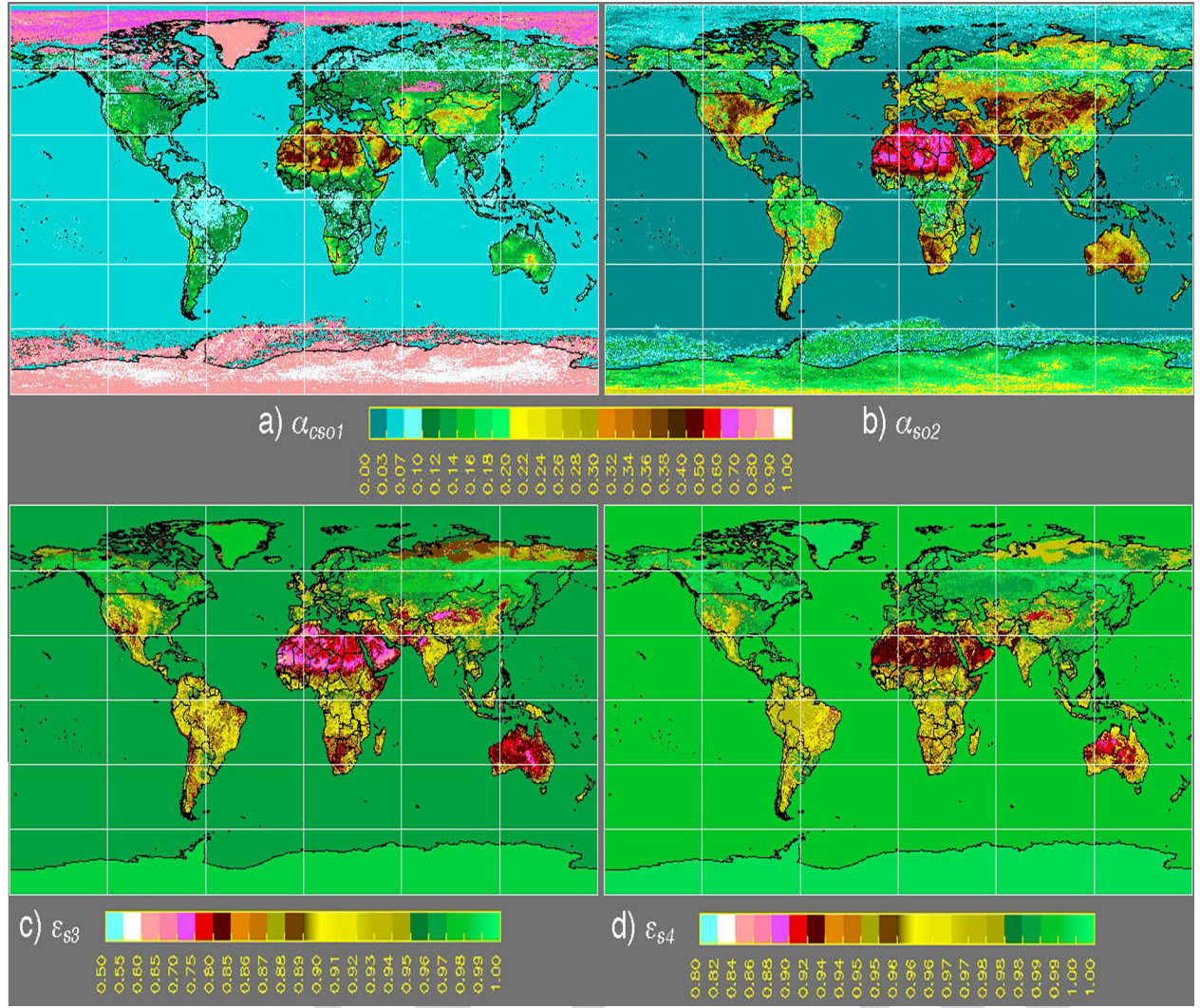
Fig. 3. CERES Terra MODIS clear radiation parameters for January 2001 mean (a) VIS clear-sky overhead-sun albedo, (b) 1.62-μm overhead-sun surface **4/C**
albedo, (c) 3.79-μm surface emissivity, and (d) 10.8-μm surface emissivity.

surface albedo data are now available from the MODIS Land
Surface science team [37], [38], they were unavailable when
these CERES algorithms were developed and applied to the
initial VIRS and MODIS data sets. Use of those surface albedos
in future CERES editions will be considered but will require
substantial modifications to the CERES algorithms.

Spectral surface emissivities $\varepsilon_{\text{S}i}(K, \lambda, \phi)$ at the 10' are used
in conjunction with the reanalysis skin temperatures to estimate
the clear-sky radiances for the CERES reference channels,
$i = 3$, 6, where the wavelengths are listed in Table I. The
CERES surface emissivity values are taken from the monthly
averages of Chen *et al.* [39], [40]. Other global surface emis-
sivity data sets (MOD11, MYD11) have become available
from the MODIS Land Surface science team [41], [42] since
CERES processing began. Although analyses using early ver-
sions of MOD11 [41] yielded predictions of spectral clear-sky
temperatures that are as accurate as those derived using the
CERES emissivities [40], the later versions [42] may yet offer
improvements for future CERES editions. For ocean surfaces,
$\varepsilon_{\text{S}4}$ and $\varepsilon_{\text{S}5}$ are set to unity because it was found that they
provide better estimates of the observed clear-sky radiance than

the model values used by Chen *et al.* [40]. During daytime,
solar radiation in the SIR channel is reflected by the surface in
addition to the thermal emission from the surface. To account
for this reflected contribution, the SIR or channel-3 surface
reflectance is estimated as

$$\rho_{\text{cs}3} = (1 - \varepsilon_{\text{S}3})\chi_{\text{s}7}(K; \mu_o, \mu, \psi)t_3. \qquad (6)$$

The BRDFs used for the 2.13-μm channel are also used for
channel 3 because of the lack of bidirectional reflectance
measurements at the SIR wavelengths. An exception is the
theoretical 3.8-μm snow reflectance model [31], which is used
here for all snow and ice surfaces.

Fig. 3 shows an example of the global maps of monthly
mean surface emissivities and overhead-sun albedos for Terra
MODIS. Note that areas with permanent snow or ice cover or
having seasonally persistent snow cover are given albedos for
snow-covered scenes. Where the snow cover is highly variable,
the albedos are initialized with the snow-free value and can vary
during a given month. Fig. 3(a) shows that some areas with
seasonal snow cover have the average snow albedos, whereas

other areas that are typically snow covered during January have the snow-free albedos. In practice, these snow-free albedos are overwritten during processing with the model snow albedos from the model whenever the ice–snow map indicates snow cover for the area. Variations in the emissivity and albedo patterns are generally related. The desert VIS albedos [Fig. 3(a)] are typically higher than those for no-snow surfaces but are less than their 1.64-μm counterparts [Fig. 3(b)]. The surface emissivities decrease with increasing VIS albedo, except over snow-covered regions. Surface emissivity at 3.8 μm [Fig. 3(c)] is typically less than that at 10.8 μm [Fig. 3(d)]. A few ε_{S3} values over the western Sahara are as low as 0.60 compared to 0.92 for ε_{S4}, which are the smallest values at 10.8 μm. The average value of ε_{S3} for the barren surfaces, 0.77, is smaller than the value of 0.88 from the MOD11 data [41], but comparable to the value of 0.76 determined from Meteosat measurements [42]. Except for some extreme values like those just noted, the CERES surface emissivity values are similar to those derived from other algorithms and data sets.

C. Fixed Ancillary Data

Average land elevation was determined for each 10' region from the 1-km United States Geophysical Survey (USGS) GTOPO30 data set (http://edc.usgs.gov/products/elevation/gtopo30/ gtopo30.html). The surface type for a given 10' region is taken from the modified IGBP map described by Sun-Mack *et al.* [31]. The percentage of water surface in a given 10' region was determined from the 1-km IGBP data set.

III. METHODOLOGIES

The CERES scene classification is one of the two main parts of the CERES cloud processing system, which is shown schematically in Fig. 4. To define a pixel as cloudy or clear (cloud mask), the system ingests the radiance and ancillary data described earlier on a pixel tile basis. Each tile consists of an array of pixels defined by 8 scan lines and 16 elements. For VIRS and MODIS, these arrays nominally correspond to 16 km $\times$ 32 km and 32 km $\times$ 32 km, respectively. Although each pixel is analyzed individually, all pixels within a given tile use the same predicted clear radiances and atmospheric corrections in the retrieval. After ingesting the input data, the expected clear-sky radiances and clear-cloudy thresholds for the tile are computed for each channel, and the observed radiances are compared to the thresholds to determine if each pixel within the tile is clear or cloudy. If cloudy, the pixel is passed to the retrieval subsystem (shaded boxes) where cloud properties are determined. If no valid results can be obtained, the pixel is given a no-retrieval classification and tested within that system to determine if it warrants a clear classification. If categorized as clear in the original mask, the pixels may be used to update the clear radiance map for a given 10' region and then are passed into the cloud property retrieval subsystem along with any cloudy pixels from the same tile. The predicted clear-sky radiances for the tile are also passed into the retrieval subsystem. These processes are described in detail in the succeeding discussions.
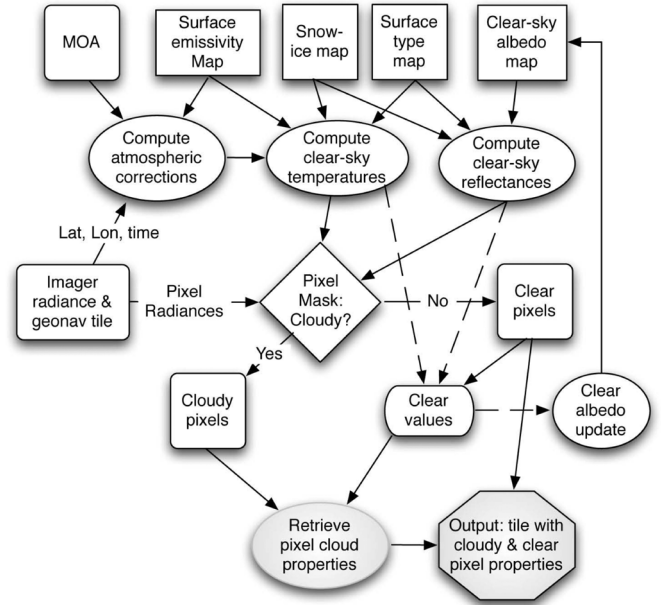

Fig. 4. Schematic diagram of CERES cloud processing system. Unshaded areas correspond to the scene identification process.

A. Clear-Sky Radiance Prediction

To compute expected clear-sky radiances, the surface emissivities, skin temperatures, atmospheric profiles, and albedos must be defined for the tile. To define the tile skin temperatures and atmospheric profiles of temperature and humidity, the code determines which 0.5° or 1° NWA grid box has its center closest to the tile center. The six-hourly profiles and three-hourly skin temperatures for that box are then linearly interpolated to the time of the satellite measurement to provide input for the clear-sky radiance and atmospheric correction calculations. Average clear-sky VIS albedos, NIR surface albedos, surface elevation, surface emissivities, water percentage, snow coverage, and albedo-weighted BRDF factors are computed using values of each parameter for all 10' regions with centers that fall within the perimeter of the tile. The dominant surface type is also identified. Similarly, the largest average 10' rms uncertainty in the box is identified in each channel. Unless otherwise noted, these average values are used hereafter in the discussion of the clear-sky radiance prediction or mask analyses.

1) VIS and NIR: The channel-1 and NIR clear-sky reflectances for each pixel are computed as in (4) and (5), respectively, using the values for χ and α corresponding to the 10' region containing the given pixel. No atmospheric corrections are applied to the VIS reflectances. The atmospheric transmittance for 1.62-μm channel is estimated as

$$t_2 = \exp\left[-\tau_2(1/\mu_o + 2.04)\right] \quad (7)$$

where τ_2 is the effective water vapor optical depth parameterized as a function of column precipitable water based on fits to adding–doubling radiative transfer computations.

2) SIR: The SIR radiance leaving the surface is approximated as

$$B_3(T_{s3}) = \varepsilon_3\left[B_3(T_{skin})\right] + \alpha_3\left(L_{a3} + \chi_3 S_3'\right) \quad (8)$$

where B_3 is the Planck function evaluated at the energy-equivalent wavelength of the channel-3 band, T_{s3} is the apparent surface temperature at 3.8 μm, L_{a3} is atmosphere-emitted downwelling radiance, and S'_3 is the solar radiance incident at the surface. The SIR surface albedo is estimated as

$$\alpha_3 = 1 - \varepsilon_3. \tag{9}$$

The incident solar radiation at the surface is computed as

$$S'_3 = \mu_o \sum_{m=1}^{5} S_{om} \Delta\lambda_m \prod_{n=19}^{1} t_{d3mn} \tag{10}$$

where S_{om} is the TOA solar radiance for wavelength interval m, where m denotes the 0.1-μm-wide subbands 1–5 for the SIR channel between 3.55 and 4.05 μm. The transmittances for each layer n to downwelling radiation t_{d3mn} are computed using the correlated k-distribution method [44] and the same coefficients employed by Minnis *et al.* [18]. These coefficients include N_2O absorption, which was not in the original set of coefficients [44]. The value of L_{a3} is estimated as the integral of the radiation emitted by each layer transmitted to the surface over all five subbands. Those calculations use the temperature and humidity profiles from the NWA interpolations. Those profiles are sometimes adjusted with the technique of Rose *et al.* [45] to ensure consistency between the observed and computed radiances. It is assumed that the surface emissivity is constant across all five subbands.

The upwelling SIR radiance at the surface $B_3(T_{s3})$ is then corrected for attenuation by the atmosphere to predict the clear-sky temperature T_{cs3}. Different sets of transmittances are computed for the upwelling radiation as a function of the pressure at the radiating surface to account for band saturation. This approach yields a mean difference between the observed and predicted values of T_{cs3} of -2 K–$+2$ K and -1 K–$+1$ K during daytime and nighttime, respectively, with standard deviations σ_3 less than 3 K and 2 K. The channel-3 clear-sky temperature uncertainties are estimated as the standard deviations between the predicted and observed temperatures with minima of 2.5 K and 3.0 K for ocean and land, respectively.

3) IR: The 10.8- and 12.0-μm TOA clear-sky temperatures, T_{cs4} and T_{cs5}, respectively, are derived in a manner similar to that for channel 3, except without the solar radiance contributions. The radiance leaving the surface is computed as in (8), except that the solar term is zero and the subscripts are replaced by 4 and 5 for 10.8 and 12.0 μm, respectively. These values are then adjusted to the TOA by accounting for gaseous absorption and emission of the atmosphere using the appropriate correlated k-distribution coefficients [18]. Channel-4 clear-sky temperature uncertainties are estimated as the standard deviations between the predicted and observed temperatures with minima of 2.5 K and 3.0 K for ocean and land, respectively. The nominal 10.8-μm uncertainty, $\sigma'_{cs4}(\lambda, \phi, m)$, is given in kelvins and is adjusted as a function of VZA to account for increases in apparent optical depth with rising VZA. The resulting uncertainty used in the clear-sky threshold is

$$\sigma_{cs4}(\lambda, \phi, m) = \sigma'_{cs4}(\lambda, \phi, m) + \text{delT}(\mu) \tag{11}$$

where $\text{delT}(\mu) = 0$ if $\mu = 1$ or if $\mu < 1$

$$\text{delT}(\mu) = 4.11 - 7.69\mu + 3.57\mu^2. \tag{12}$$

To ensure consistency between using the ECMWF for VIRS and GEOS for MODIS analyses, six days of 2001 Terra MODIS data from the four seasons were analyzed separately using ECMWF and GEOS profiles as input. In general, it was found that cloud amounts derived using GEOS as input differed by less than ±0.006, on average, compared to those based on the ECMWF data. At night, however, the land skin temperatures were greater than those from ECMWF, resulting in an overestimate of cloudiness at night. Fig. 5 shows an example of the differences between the predicted clear-sky temperatures from ECMWF and GEOS and the observed 10.8-μm brightness temperatures and the ensuing cloud mask for an area in southern Asia for Terra MODIS data taken at 1650 UTC on January 3, 2001. The GEOS 4.03 predicted values [Fig. 5(b)] are more than 7.5 K greater than the observed values over central India compared to ECMWF [Fig. 5(a)], which has maximum differences of less than 5 K in that same area. The result is false cloud detection using GEOS 4.03 [Fig. 5(d)] for that area compared to the minimal detection of clouds there when ECMWF temperatures are used [Fig. 5(c)]. Globally, no changes were made to the thresholds over ocean and daytime land. At night, the IR thresholds were increased by 30% over land to minimize the effects of differences in skin temperature between ECMWF and GEOS 4.03.

B. Nonpolar Scene Identification

The CERES cloud mask consists primarily of cascading threshold tests. To define a pixel as cloudy, at least, one of its five spectral radiances must differ significantly from the corresponding expected clear-sky radiances. A cloudy pixel may be classified as good or weak depending on how much the radiances differ from the predicted clear-sky radiances. Pixels identified as clear are designated as weak or good or categorized as being filled with smoke, fire, or aerosol, contaminated by sunglint, or covered with snow. These qualifiers for the basic classifications provide information for assessing the certainty of the retrieval or for explaining why the classification may differ from expected values. For VIRS, the daytime (SZA $< 82°$) masking algorithm can use all five channels, whereas the nighttime technique only employs channels 3, 4, and 5. A few extra channels are used for the MODIS processing (see Table I). Polar regions are defined as all areas poleward of 60° latitude and all areas between 50° and 60° latitude where the snow–ice maps indicate that the surface is covered with snow or ice. The nonpolar masks apply to all other areas. Although the cascade logic and some of the tests to discriminate clear from cloudy pixels are different, much of the theoretical basis and details of some tests are given by Baum *et al.* [46].

1) Daytime: Every nonpolar pixel is classified during daylight using a sequence of tests as shown in Fig. 6. The first check, or **A** test, identifies all pixels that are obviously too cold to be cloud free. If $T_4 < T_{lim}$, then the pixel is designated a good cloud. For VIRS Ed2, this test was called without
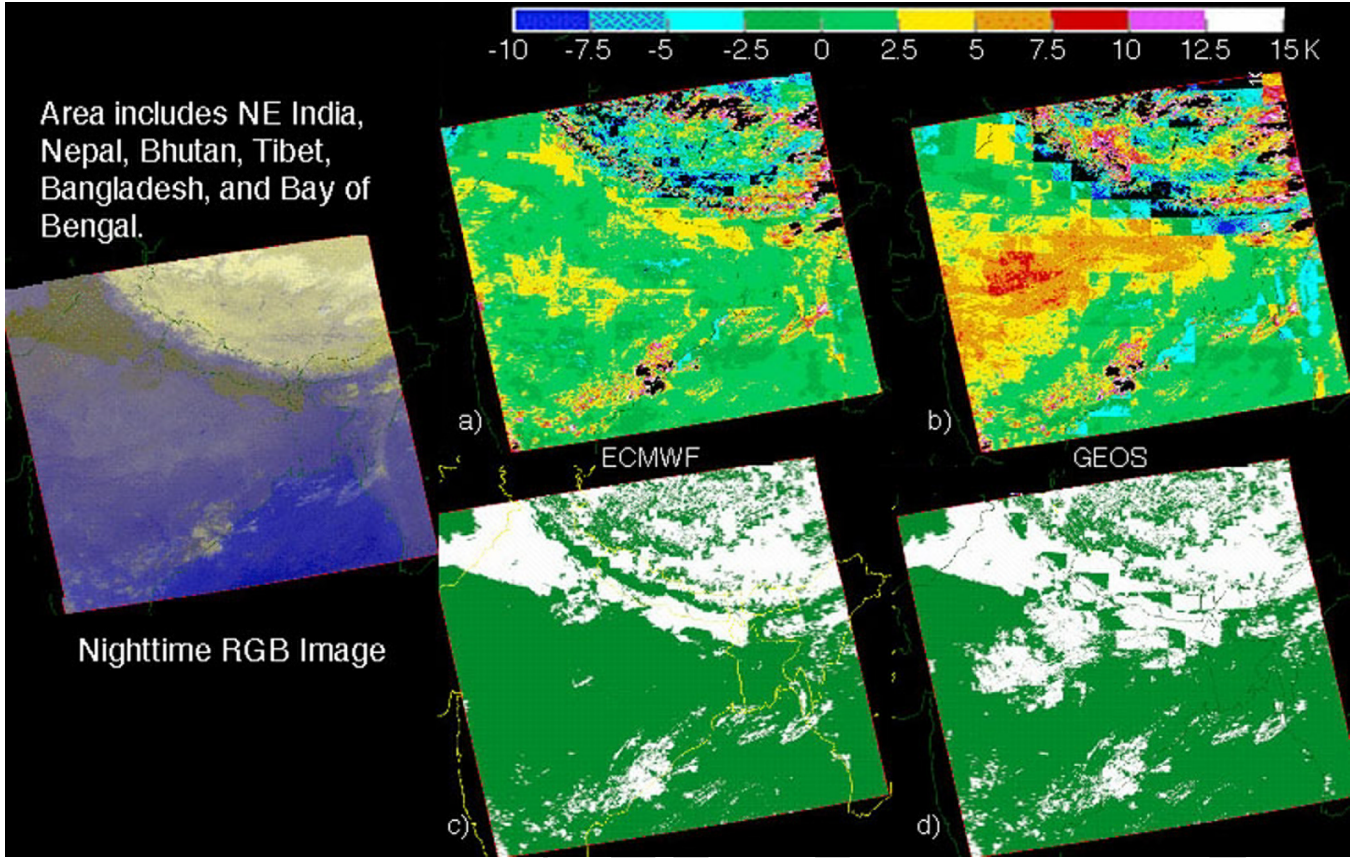
Fig. 5. Comparison of nighttime cloud mask for Terra MODIS over southern Asia 1630 UTC, January 3, 2001. Differences between observed and predicted clear-sky IR brightness temperatures: (a) ECMWF and (b) GEOS 4.03. Cloud mask using (c) ECMWF and (d) GEOS 4.03 skin temperatures. Black areas are off scale. Note that the more apparent blockiness in the GEOS temperature differences results from the GEOS lower (1°) spatial resolution relative to the 0.5° ECMWF resolution.

restrictions, and the value of $T_{\lim}$ is equal to the temperature at 500 hPa over land or to 260 K over ocean. In the MODIS processing, the test is not used if $T_{\rm skin} < 270$ K or the surface elevation exceeds 4 km.

If the pixel is not cloudy after the **A** test, it is then compared against the expected clear-sky radiances in the following **B** tests, where the parameters **B1**, **B2**, and **B3** are initialized to zero:

$$\text{If} \quad T_4 < T_{\rm cs4} - \sigma_{\rm cs4} \qquad B1 = 1 \tag{13a}$$

$$\text{If} \quad \rho_1 > \rho_{\rm cs1}(1 + \sigma_{\rm cs1}) \qquad B2 = 1 \tag{13b}$$

$$\text{If} \quad \text{BTD}_{34} > \text{BTD}_{\rm cs34} + \sigma_{\rm cs34} \qquad B3 = 1. \tag{13c}$$

In these equations, the subscript numbers refer to channel number, and the subscript cs denotes the predicted clear-sky value. When two channels are indicated, the parameter is either the ratio of or the difference between the two channels, e.g., BTD_{34} is the observed BTD between channels 3 and 4. If the sum of the **B** parameters is zero or three, then the pixel is initially identified as good clear or cloudy. If certain conditions are met, the pixel may be reclassified after passing through a set of **ALL B** clear or cloudy tests shown in Fig. 6. The former checks spectral consistency in glint-free or sunglint conditions over ocean using sunglint probability (SGP) or tests

for shadows over land [Fig. 7(a)], whereas the latter checks for other effects on the assumed thresholds as a result of sunglint or highly reflective desert surfaces [Fig. 7(b)]. These **ALL B** tests use a variety of parameters including observed reflectance ratios $R_{ij} = \rho_i/\rho_j$ and constraint reflectance ratios r_{ij}, where i and j are channel numbers. The constraints are defined for sunglint, indicated with the subscript g, and other conditions are denoted by the subscript c. For Aqua, channel 7 is used instead of channel 2. These defining reflectance ratio values are listed in Table III. The initial **B** result is the final classification unless the **ALL B** tests change it. If the sum of the **B** parameters is either one or two (Fig. 6), then a thin cirrus test is applied (Aqua Ed1 only) followed by one of six sets of **C** tests that depends on which **B** tests failed and on the surface type. The Aqua thin cirrus tests, shown in Fig. 8, were developed after visual examination of the Terra Ed2 results revealed that thin cirrus clouds were being missed in some instances when they should have been detected. These tests utilize the 1.38-μm reflectance ρ_8 and the 8.55-μm brightness temperature in the form of BTD_{64}, as well as BTD_{45}. Several constraint parameters are used that depend on the precipitable water vapor, which is indicated by the subscript PW. A cruder version of the thin cirrus test was applied in some of the **C** tests for all satellites.

The **C** tests adjust the clear-sky uncertainties and may also involve channels 2 or 5 in addition to the three channels used
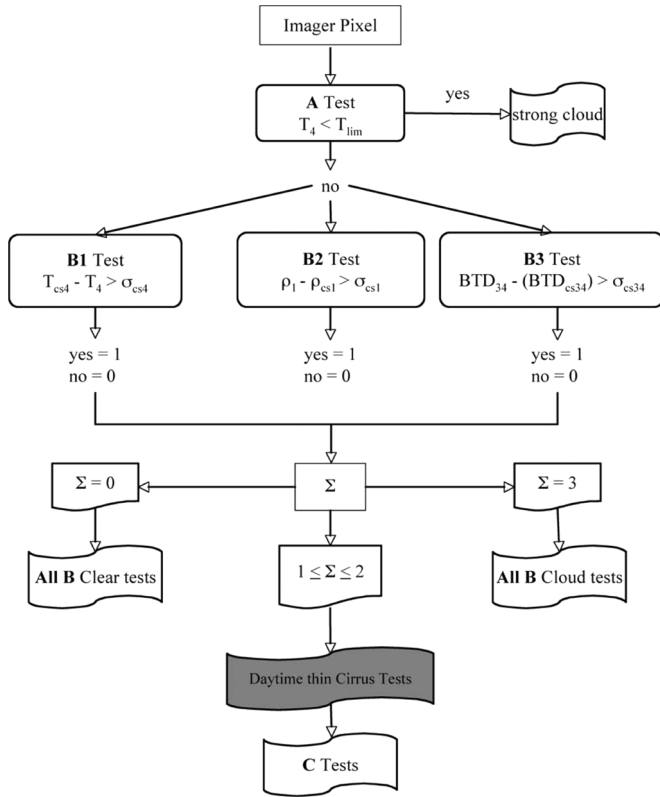
Fig. 6.   Outline of daytime scene identification process. Shading indicates use in Aqua Ed1a only.

in the **B** tests. For example, if the scene is bright and cold over land, the **C** test will check for snow using the expected snow reflectance ratio R_{21} of 1.6–0.64 μm. From these **C** tests, a pixel categorized as clear may be assigned additional classifiers such as good, weak, snow, aerosol, smoke, fire, or glint. Cloudy pixels may be classified as good, weak, or glint. Fig. 9 shows one of the six **C** tests, **C1**, which is called when the IR test fails ($B1 = 0$). Over land [Fig. 9(a)], the VIS and BTD$_{34}$ thresholds are relaxed by a factor of two and by a variable relaxation factor f_r, respectively. The value of f_r is 2.0 for desert areas and 1.5 for vegetated land areas. If both tests are passed, the results are tested for snow using a temperature and reflectance ratio tests. If positive snow does not result, the pixel is classified as weak or good cloud depending on the temperature and the reflectance ratio R_{21}. If only the VIS test is passed, the radiances are tested for snow. If no snow, then a test for smoke is applied by further increasing the VIS threshold. If no smoke is detected, then the pixel is classified as weak or good cloud. Similarly, if only the BTD$_{34}$ test is passed, then the cloud is classified as weak or good depending on R_{21}. If both tests fail, then the radiances are examined to determine if the pixel should be classified as clear good, weak, smoke, or fire.

Over ocean [Fig. 9(b)], the SGP is tested to determine if there is any likelihood of sunglint affecting the clear reflectances. If SGP exceeds 40%, then the sunglint tests shown in Fig. 10 are applied. The clear sunglint tests rely on the spectral reflectance ratio R_{31}, the VIS reflectance, and the IR or SIR temperatures. The cloud tests depend on T_4 and BTD$_{34}$. The latter is

compared to the sum of two uncertainties: the BTD$_{34}$ sunglint uncertainty

$$\sigma_{cs34g} = 4.316 \text{ K} + 0.123 \text{ K SGP} \qquad (14)$$

and the nighttime high-cloud BTD$_{34}$ uncertainty σ_{cs34hi}. The latter is simply the daytime uncertainty with the reflectance components removed. If the sunglint tests fail for the strong sunglint cases [Fig. 9(b)], then a final test is applied using two spectral reflectance ratios. When SGP falls between 2% and 40%, moderate sunglint tests are invoked using looser BTD$_{34}$ and VIS reflectance uncertainties. Again, spectral reflectance ratios are used to determine a classification. For nonglint cases, SGP $< 2\%$, a set of tests is applied to determine if aerosols can be causing the enhanced reflectances. Reflectance ratios T_4 and an enhanced BTD$_{34}$ uncertainty are used to detect aerosols. If the aerosol tests are not passed, then the thresholds for VIS and BTD$_{34}$ are enhanced and applied in fashion similar to that for the land cases. The pixel is good cloud only if both tests are passed. Because of the obvious complexity of the **C** tests and the number of required diagrams, only **C1** is illustrated here. More details, as well as the flowcharts for the remaining five **C** tests (**C2**–**C6**), are provided elsewhere (http://www-angler.larc.nasa.gov /CERES_algorithms/).

An example of predicting the clear-sky VIS reflectances for the daytime mask is shown in Fig. 11 for data taken around 17 UTC on December 21, 2000 over the southwestern USA and northern Mexico. The three-channel Terra MODIS image [Fig. 11(a)] shows green and bluish areas that are clear land and desert. Dark areas are clear water, whereas white, gray, pink, and yellow areas correspond to clouds. The bright magenta areas are covered with snow. Some of the input data, such as radiances, water percentage, snow/ice, and clear-sky overhead albedo, are shown in Fig. 11(a)–(d), respectively. The computed directional reflectance model values [Fig. 11(e)] applied to the overhead-sun albedos yield the clear-sky albedos at the image time [Fig. 11(f)]. These are multiplied by the BRDF factors [Fig. 11(g)] to obtain the predicted clear-sky VIS reflectances [Fig. 11(h)]. When compared to the observed VIS reflectance in Fig. 11(i), it is apparent that in areas where it is visually cloudy or snow free, ρ_{cs1} is reasonably close to the observed value.

The corresponding processes for estimating T_{cs4} and BTD$_{cs34}$ are shown in Fig. 12. The MOA skin temperatures [Fig. 12(b)] are given at the 1° scale and used with the MOA temperature and humidity profiles (PW in Fig. 12(c) illustrates the variability in humidity) and the surface emissivities [Fig. 12(d) and (g)] taken from maps like those in Fig. 4(c) and (d) to compute the clear-sky brightness temperatures. The values of T_{cs4} in Fig. 12(e) were computed at the tile scale and tend to be less than the observed values [Fig. 12(f)] over land and slightly higher over water. This difference can mostly be attributed to the MOA skin temperatures since they are typically less than the observed clear-sky temperatures even before the surface emissivity and atmospheric corrections reduce T_{skin} to T_{cs4}. The values of BTD$_{34}$ [Fig. 12(h)] are greater than the observed values [Fig. 12(i)] in some clear areas and less than the values in other areas. The observations do not show the same degree of VZA dependence over water that is predicted.

(a) All **B** good clear

Confirm good clear over non glint ocean

SGP = 0
$R_{21} > 0.30\, r_{21c}$ &
$\rho_2 - \rho_{cs2} > 0.5\, \sigma_{cs2}$

→ yes → cloud weak

Confirm good clear over moderate sun glint ocean

SGP < 20%
$R_{23} > 0.95$ & $\rho_2 - \rho_{cs2} > 3\sigma_{cs2}$

→ yes → cloud weak

Shadow tests over land

$\rho_2 - \rho_{cs2} < -0.05_2$ & $\rho_1 < \rho_{cs}$ & $_1$
$T_{cs4} - T_4 > 0$

→ yes → clear shadow

(b) All **B** good cloud

Confirm good clouds over strong sun glint ocean

SGP > 40%
$R_{23} < r_{23g}\, r_{21c}$ &
$R_{13} < 1.3$ & $T_{cs4} - T_4 < 7.5K$ &
$BTD_{45} < thrCi$

→ yes → clear glint

Confirm good clouds over desert

$R_{21} > 1.3\, r_{12c}$ & $R_{13} < 2.5$ &
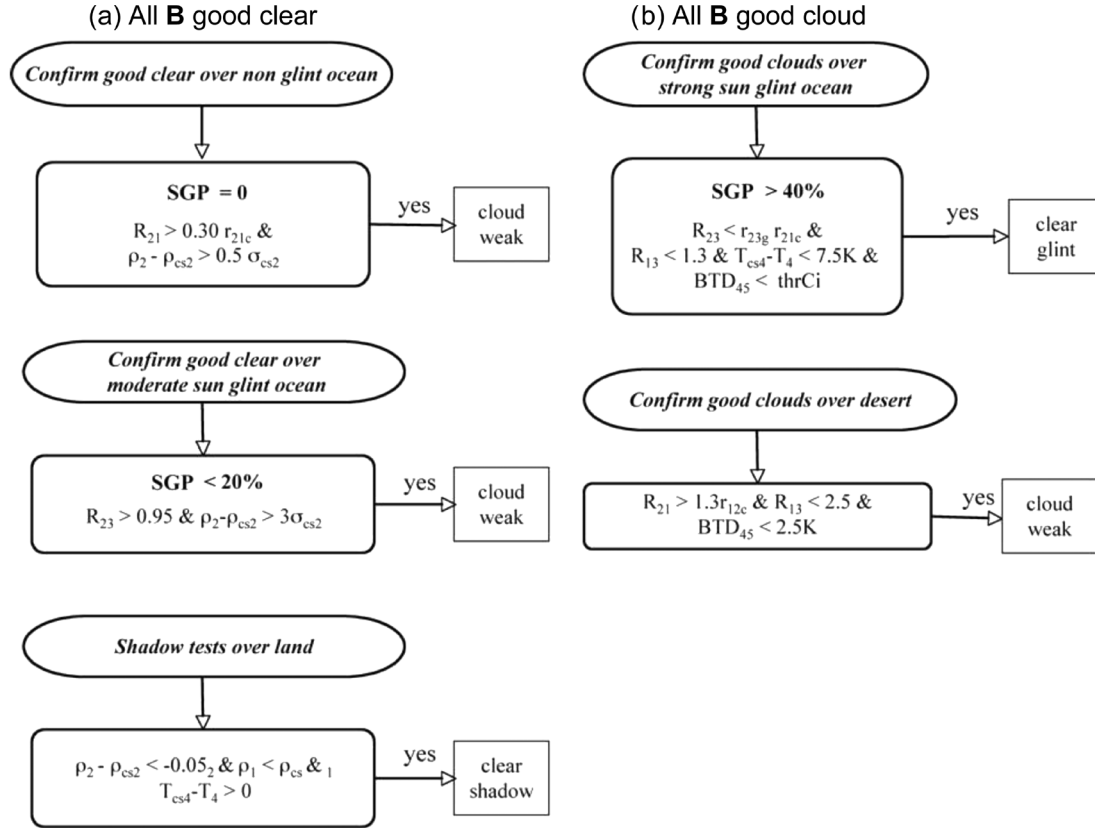$BTD_{45} < 2.5K$

→ yes → cloud weak

Fig. 7. Final classification for certain pixels classified as (a) clear or (b) cloudy after all of the **B** tests. If the specified conditions are met, the pixel is reclassified. SGP refers to sunglint probability.

TABLE III
CONSTRAINT VALUES FOR REFLECTANCE RATIO TESTS

Parameter	Conditions	Formula
r_{23g}	sunglint	$r_{23g} = 0.005\ SGP + 1$
r_{21c}	sun glint ocean	$r_{21c} = 0.18\ \mu + 0.625$
r_{21c}	non-glint ocean	$r_{21c} = 0.20\ \mu + 0.587$
r_{21c}	desert	$r_{21c} = 0.843$
r_{21c}	non-desert land	$r_{21c} = 0.572$
r_{21c}	Non-polar snow	$r_{21c} = 044$

Land

$\rho_8 > \rho_{8PW} + 0.002$ → $F_8 = 1$

$BTD_{45} > T_{45PW}$ → yes → $F_{45} = 1$

$BTD_{64} > T_{64PW} + 1$ → yes → $F_{64} = 1$

$F_{\rho 8} = 1$ & $F_{45} = 1$ & $F_{64} = 1$ & $BTD_{34} - BTD_{cs34} > 1.0K$

→ Thin Ci clouds

Ocean

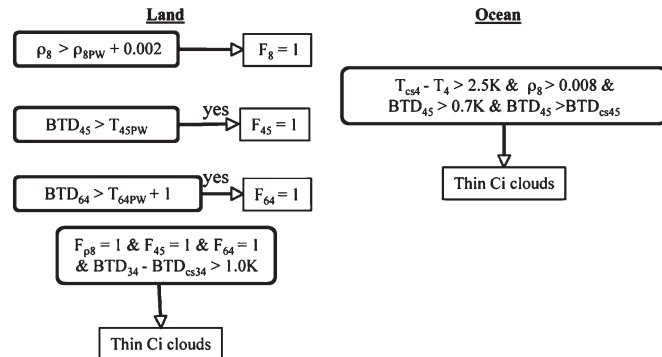$T_{cs4} - T_4 > 2.5K$ & $\rho_8 > 0.008$ & $BTD_{45} > 0.7K$ & $BTD_{45} > BTD_{cs45}$

→ Thin Ci clouds

Fig. 8. Thin cirrus tests used for Aqua Ed1a processing after **B** tests are applied.

Using these clear-sky values in the daytime cloud mask yields the results shown in Fig. 13. The **ABC** summary [Fig. 13(a)] shows examples of the various tests that were used to classify the clouds. While a few snow-covered regions are shown in yellow because the pixels passed **B1** and **B2**, most are blue having passed only **B2** because T_{cs4} is less than T_4 [Fig. 12(e)–(f)]. A large part of the desert and shadowed areas passed **B1** but failed the other two. Only a few areas of high clouds passed the **A** test (white), whereas many of the clouds over the Rocky Mountains and the Gulf of Mexico passed all three **B** tests (gray). The other colors indicate the final tests used to classify the pixels.

The cloudy pixels [Fig. 13(b)] are identified as good (white), weak (pink), or no retrieval (blue). The last category indicates that those pixels that were identified as cloudy have radiances that cannot produce solutions to the models used in the cloud retrieval program [14], [47]. Typically, no-retrieval cloudy pixels are reclassified as clear in the cloud retrieval portion of the system using an additional mask developed by Welch *et al.* [48]. The clouds over the snowy areas and over the southeastern part of the image appear to be properly classified when compared with the composite image in Fig. 12(a). The cloudy areas over northeastern Mexico, southern Texas, and near the Arizona–New Mexico border are difficult to see in Fig. 12(a), but they appear as relatively cold areas in Fig. 12(f) and as warmer areas (larger BTD_{34}) in Fig. 12(i). Those characteristics are typical of thin cirrus clouds. Weak clouds are detected near the thin cirrus clouds and over the Pacific and Sea of Cortez where the clouds are very faint in the image. The no-retrieval pixels occur along the edges of the snowy areas and the thin cirrus regions. Although some likely clear pixels along the snow edges are misclassified as good clouds,

b: $\rho_1 - \rho_{cs1} > 2\sigma_{cs1}$
c: $BTD_{34} - BTD_{cs34} > f_r\sigma_{cs34hi}$
yes = 1   no = 0

$b=1$ $c=1$ $b=1$ $c=0$ $b=0$ $c=1$ $b=0$ $c=0$

snow tests
$R_{21} < 0.40r_{21c}$ &
$T_4 (T_{skin}) < 277K$ &
$BTD_{34} - BTD_{cs34}$
$< 2\sigma_{cs34hi}$

no → yes → clear snow

snow tests
$R_{21} < 0.40r_{21c}$ &
$T_4 < 277K$

no   yes

smoke tests over forest
$T_{cs4} - T_4 > 0.5\sigma_{cs4}$

yes → clear smoke   no → clear weak

$R_{21} < 1.4r_{21c}$
or
$T_{cs4} - T_4 > 0.5\sigma_{cs4}$

yes → cloud good   no → cloud weak

smoke tests over forest
$\rho_1 - \rho_{cs1} < 3\sigma_{cs1}$

yes → clear smoke   no

clear snow

$R_{21} < 1.4r_{21c}$ &
$T_{cs4} - T_4 > 0.5\sigma_{cs4}$

yes → cloud good   no → clear weak

fire tests over forest
$T_3 > 314\,K$ & $BTD_{34} > 10K$
$\rho_1 - \rho_{cs1} < 2\sigma_{\rho cs1}$

yes → clear fire

confirm weak cloud over barren desert
$R_{21} > 1.3r_{21}$ &
$R_{13} > 2.5$ & $BTD_{45} < 2.5K$

yes → clear weak

(a)

$SGP > 40\%$ — yes → **strong Sun glint** Apply SunGlintTest → cloud glint

no

$2\% < SGP < 40\%$

yes   no

fail

$R_{23} > 1.5r_{21c}$
& $R_{13} > 1.5$

no → clear glint   yes → cloud glint

moderate Sun glint
b: $\rho_1 - \rho_{cs1} > 2\sigma_{cs1}$
c: $BTD_{34} - BTD_{cs34} > 2\sigma_{cs34hi}$
yes = 1   no = 0

$b=1$ $c=1$ $b=1$ $c=0$ $b=0$ $c=1$ $b=0$ $c=0$

$R_{23} > 1.2r_{21c}$

no → cloud glint

$R_{13} > 1.4$
$R_{23} > r_{21c}$

no → clear weak   yes → cloud weak

clear glint

non glint

ocean smoke test
$0.12r_{21c} < R_{21} < 0.35r_{21c}$ &
$R_{23} > 0.5r_{21c}$ & $R_{13} > 2.5$ &
$BTD_{34} < 6.5$ & $T_4 > 278$

→ clear aerosol

no

no Sun glint
b: $\rho_1 - \rho_{cs1} > 1.5\sigma_{cs1}$
c: $BTD_{34} - BTD_{cs34} > 1.5\sigma_{cs34hi}$
yes = 1   no = 0

$b=1$ $c=1$ $b=1$ $c=0$ $b=0$ $c=1$ $b=0$ $c=0$

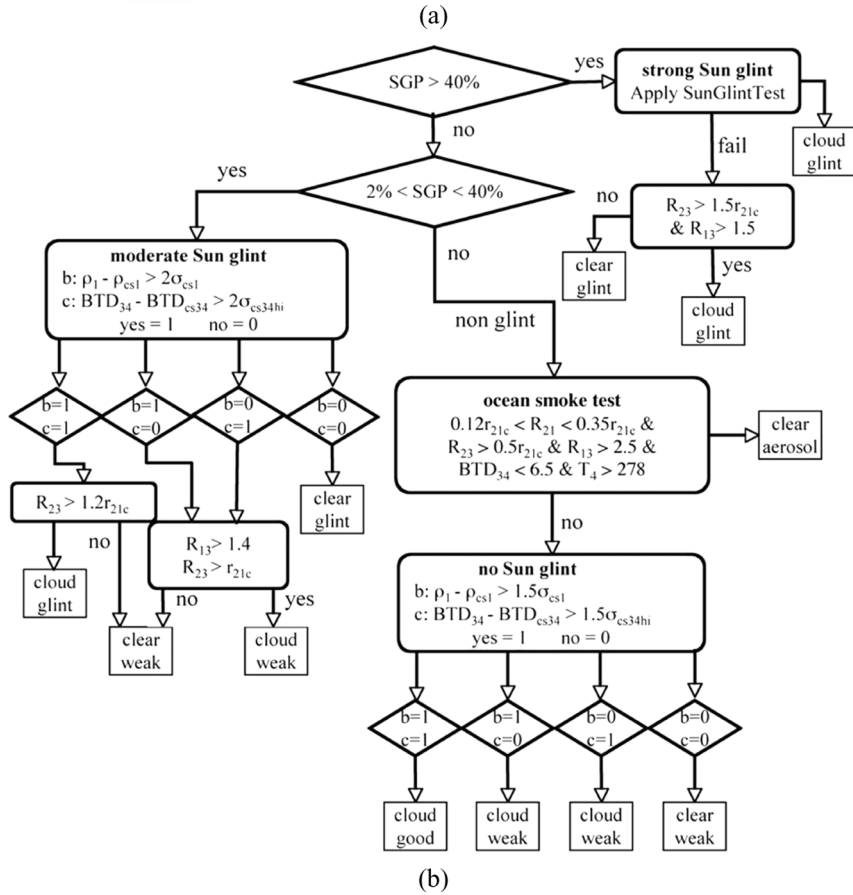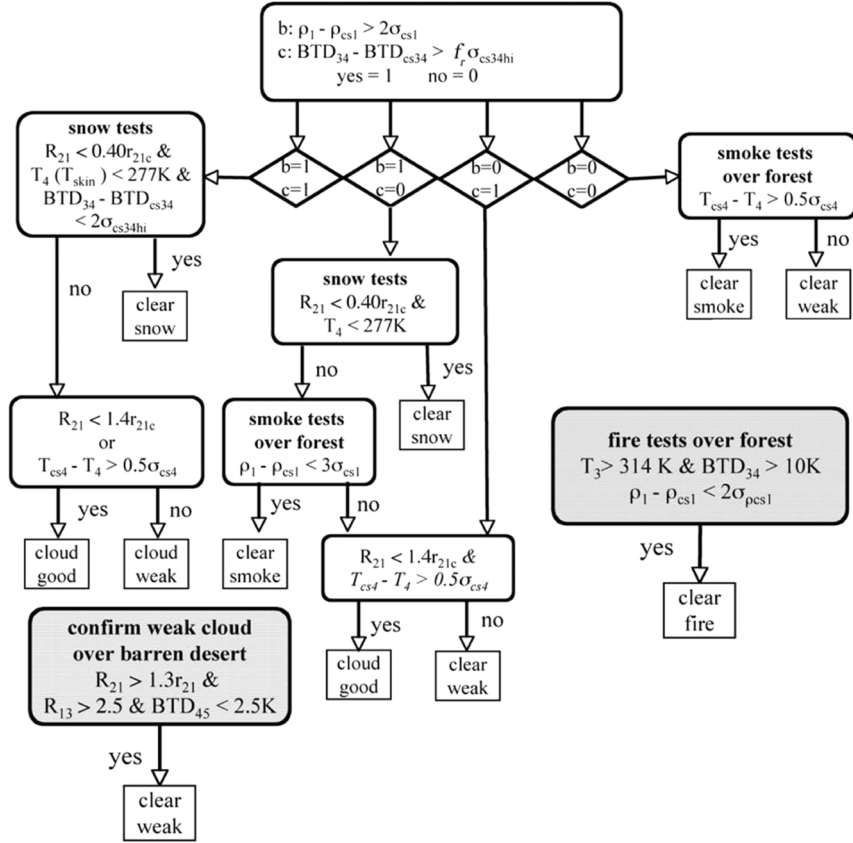cloud good   cloud weak   cloud weak   clear weak

(b)

Fig. 9. (a) Daytime, **C1** test over land. $B1 = 0$, $B2 = 1$, and $B3 = 1$. The relaxation factor f_r is 2.0 for desert and 1.5 for nondesert land. Parameters shown in italics indicate tests only used by Aqua Ed1. The T_{skin} test for $b = 1$ and $c = 1$ is only used for Terra Ed2. The free-floating tests are applied only to certain surface types after the **C1** tests are completed. (b) Same as (a), except over ocean.
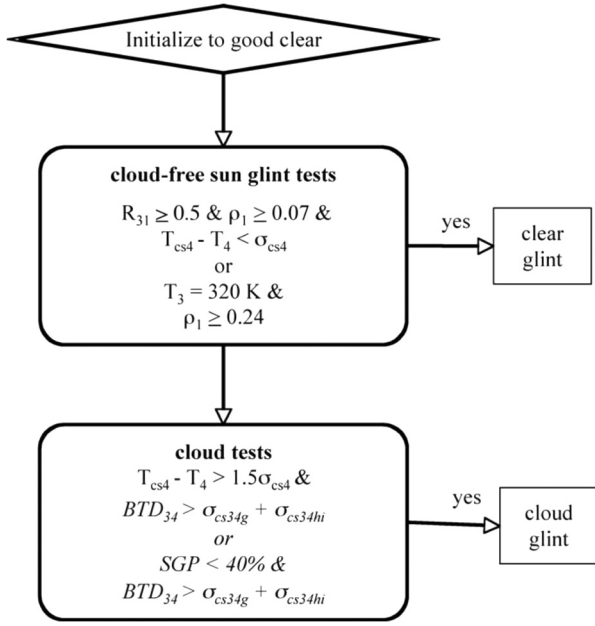
Fig. 10. Ocean sunglint tests. Italics denote tests only used for Aqua Ed1.

overall, the mask [Fig. 13(c)] appears to correctly identify most pixels.

The resulting clear pixels [Fig. 13(d)] are classified as weak (light green), good (dark green), aerosol (pink), and snow (white). The gray areas correspond to clouds. The clear areas are mostly good. Some shadowed pixels are identified over Louisiana (center right) next to the cloud edges. The snow-covered areas correspond roughly to those in the snow map [Fig. 11(b)], but some additional areas are added east of the western section and around the northwestern and southern edges of the eastern section. Much additional detail is resolved relative to the snow-map snow areas, and some snowy parts in Fig. 11(b) are reclassified as good clear, e.g., the region in the northwest corner of the image.

2) Nighttime: The nighttime mask is similar to the daytime cascade of tests. The **A** test (Fig. 14) is followed by **D** tests that begin with $D1 = D2 = D3 = 0$. The **D1** and **D2** tests are the same as **B1** and **B3**, respectively. The threshold for the **D2** test, however, uses the nighttime threshold for high clouds BTD_{cs34hi}. Because low clouds are often indistinguishable from clear skies at night in channel 4 and BTD_{34} is often negative [49], the **D3** test is used to detect low clouds by checking for smaller-than-expected values of BTD_{34}. In this test, $BTD_{34} - BTD_{cs34}$ is compared to σ_{cs34lo}, which is equal to $0.5 - BTD_{cs34hi}$. If any of the **D** tests passes, then one of the five **E** tests is applied that involves refined thresholds and channel-5 radiances. Otherwise, the pixel is passed on to the **ALL D** clear tests that are applied only in the twilight zone, the sunlit portion near the terminator, which is defined as the area where $82° < SZA < 87.5°$. At these high SZA's, the reflectance component in channel 3 is often just large enough to offset the negative BTD_{34} seen for low clouds at night, but is not sufficient to produce a strongly positive value typical of low clouds during the daytime. Thus, the additional tests, shown in Fig. 15, are invoked. Over ocean, VIS and NIR reflectances that are both significantly greater than the

predicted clear sky values will cause the pixel to be reclassified as weak cloud. To be recategorized as weak cloud over land, the observed reflectances must both exceed 0.20, and the BTD_{34} must be outside of the range between -1 K and 4 K. If no reclassification occurs, the pixel remains as good clear. Similar to the daytime **C** tests, the **E** tests, applied to the remaining pixels, change the uncertainties to yield good or weak clear or good or weak cloudy classifications.

Fig. 16 shows the outline of the **E3** test, which is invoked when **D2** is passed. That is, T_4 is higher than expected and BTD_{34} is greater than the expected clear-sky value. The channel-4 and BTD_{34} uncertainties are decreased and increased, respectively. If the observations pass both tests, then the pixel is a good cloud over ocean but undergoes one more test, using BTD_{45}, over land to see if thin cirrus caused the greater-than-expected BTD_{34} value. If only one of the two **E3** tests passes, then, over ocean, the pixel is a weak cloud if the channel-4 test passes and weak clear if BTD_{34} test passes. For land scenes, the thin cirrus (**Ci**) test is applied. This test classifies a pixel as thin cirrus if BTD_{45} exceeds threshold values that depend on VZA and T_4. The threshold values were originally developed by Saunders and Kriebel [50]. The bases for the test and the threshold values are discussed by Baum *et al.* [46]. If neither **E1** test is passed, the **Ci** test is applied regardless of surface type. As in the case of the **C** tests, only one example of the **E** tests is shown here for brevity. The details of the remaining **E** tests, **E2–E5**, can be found elsewhere (http://www-angler.larc.nasa.gov/CERES_algorithms/).

Fig. 17 shows the results of applying this classification scheme to VIRS data taken over Texas at 6 UTC on March 25, 2001. The three-channel IR pseudocolor image [Fig. 17(a)] renders clear areas in blues and tans and cloudy pixels in colors ranging from gold to white. The 3.7-μm surface emissivity [Fig. 17(g)] is generally defined only at the 0.5° scale, although some 10' regional variability is evident. It tends to increase from the forested eastern areas to the high plains in the west. Fig. 17(e) shows the BTD_{34} values ranging from less than -5 K to more than 20 K. The negative values generally correspond to low clouds, whereas the greater positive values are associated with thin high clouds. Clear areas typically have values near zero. Observed BTD_{45} values are given in Fig. 17(f), where low clouds and clear areas have values of $+1$ K and high clouds have positive values of up to 4 K or greater. The low clouds also tend to have 11-μm temperatures comparable to the clear areas [Fig. 17(d)]. The resulting cloud mask and summary of nighttime tests are shown in Fig. 17(b) and (c), respectively. The **A** test (white in summary) and the **E1** test (light blue) pick up many of the thick and thin high clouds. The **E3** test (red) detects many of the thinnest cirrus clouds, particularly those around the edges of those detected by the **E1** test. Thicker midlevel and cirrus clouds over low clouds are found using the **E5** test. In those instances, the BTD_{34} values are similar to the expected clear temperature differences. Very low or subinversion clouds were classified with the **E2** and **E4** tests. The **ALL D** clear category is indicated in green. Other clear areas were classified with the **E** tests. In some instances, it appears that cloudy pixels were misclassified as clear. These were mainly low clouds that
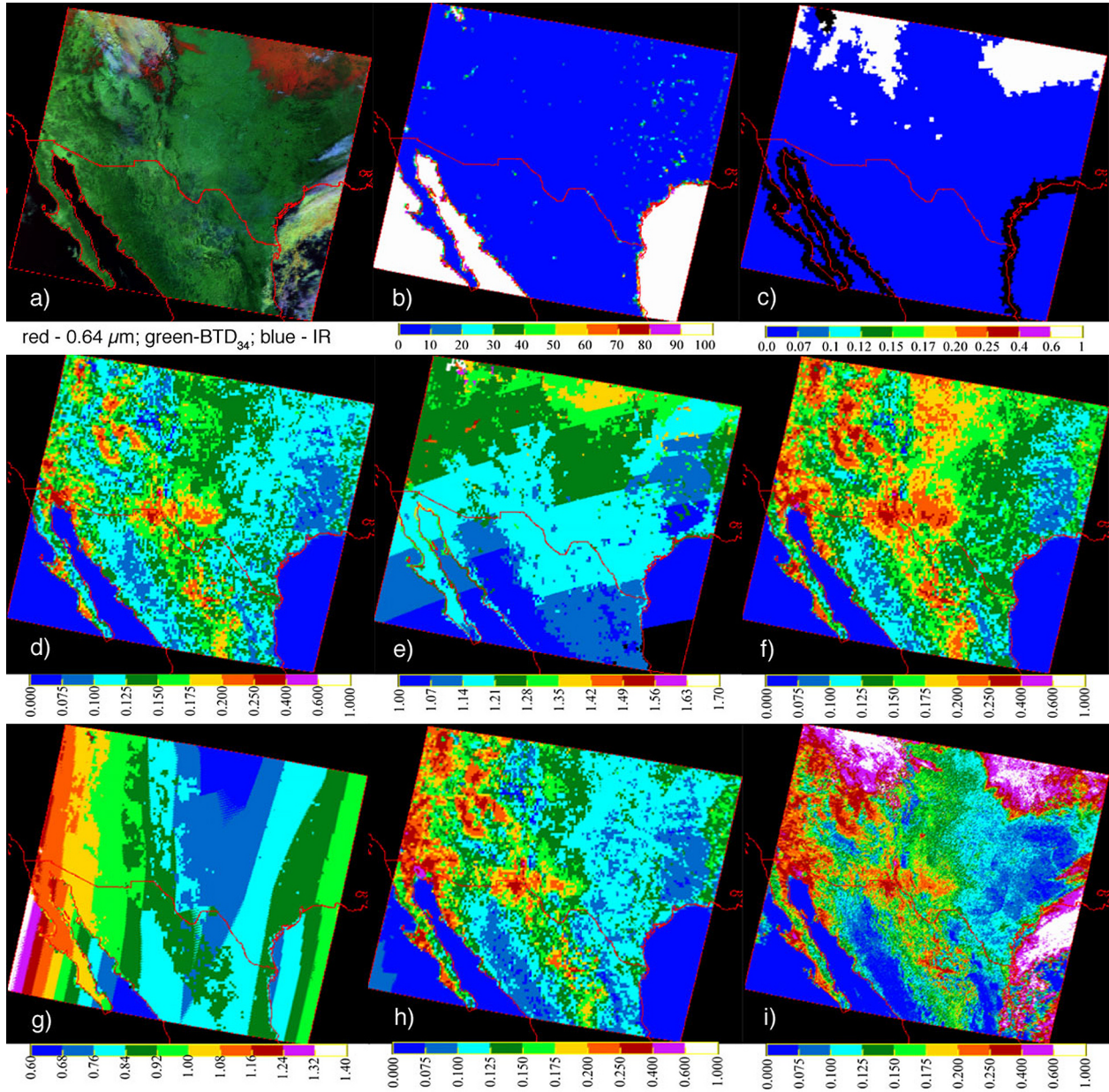
red - 0.64 μm; green-BTD$_{34}$; blue - IR

Fig. 11.   Terra MODIS image and VIS reflectance and mask input and clear-sky VIS parameters, 1700 UTC, December 21, 2000. (a) RGB image, (b) water percentage map, (c) snow–ice map, (d) overhead-sun clear-sky albedo, (e) normalized directional reflectance, (f) clear-sky albedo, (g) BRDF factor, (h) predicted clear-sky reflectance, and (i) observed reflectance.

were warm and had BTD$_{34}$ values close to the expected clear levels. They can be seen by comparing the areas where **E** tests were applied with cloudy areas in the CERES mask image. Visually, the results are quite reasonable despite a few missed clouds.

IV. RESULTS AND DISCUSSION

As noted earlier, the CERES nonpolar scene identification mask was applied to several years of VIRS data and, along with the CERES polar mask [13], [51], to long periods of Terra and Aqua MODIS data. A few examples summarizing the results are presented and discussed here.

A. Scene Identification Statistics

Tables IV and V summarize, for day and night, respectively, the relative frequency of the various tests that resulted in a final classification for all of the nonpolar Terra MODIS pixels on March 2000. During daytime (Table IV), the **A** test accounts for nearly 43% of the decisions; more occur over ocean than over land and desert surfaces. The **All B** tests result in a classification for almost 40% of the pixels, leaving only 20% to be categorized by the **C** tests. The **All B** clear classification is most common over desert areas, whereas **All B** clouds occur most frequently over ocean. The channels that are used in each **C** test are noted in the first column of Table IV. The **C5** test, in which only the IR channel indicates clouds, is invoked least often of all of the **C** tests. Bad data are those pixels having
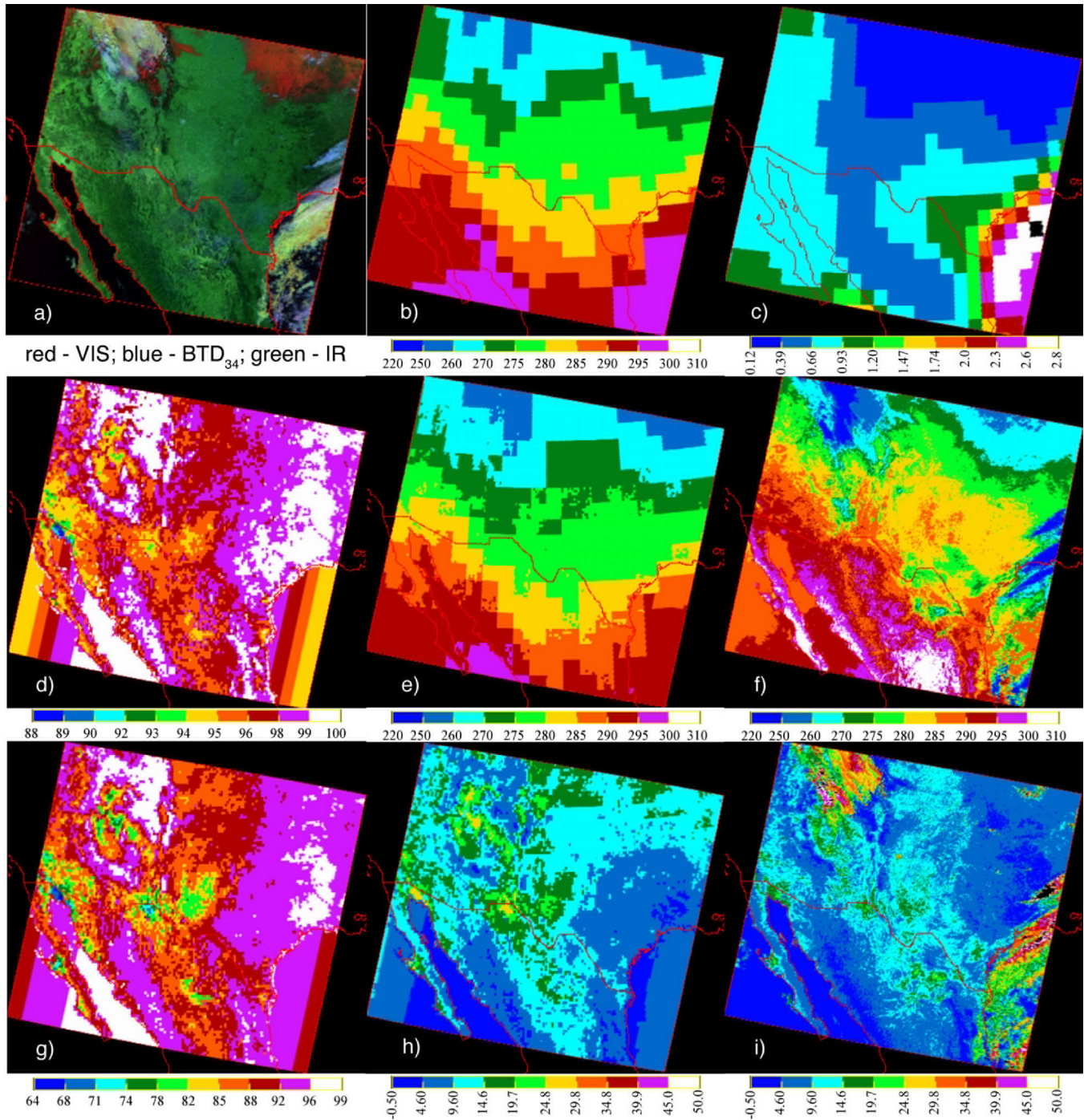
red - VIS; blue - BTD$_{34}$; green - IR

Fig. 12. Terra MODIS image, IR temperature, and BTD and mask input and predicted clear-sky IR and BTD parameters, 1700 UTC, December 21, 2000. (a) RGB image, (b) MOA skin temperature, (c) MOA precipitable water vapor in centimeters, (d) IR surface emissivity, (e) predicted clear-sky IR brightness temperature T_{cs4}, (f) observed IR brightness temperature, (g) 3.8-μm surface emissivity, (h) predicted clear-sky BTD$_{cs34}$, and (i) observed BTD$_{34}$.

4/C

932 out-of-range or saturated radiances in any of the channels used
933 in the mask. They occur mostly over land and account for 1%
934 of pixels overall.

935 At night (Table V), the frequency of positive (cloudy) **A**
936 tests is nearly the same as during the daytime, whereas the
937 **ALL D** clear occurrences are slightly greater than their daytime
938 **ALL B** counterparts. In contrast to daytime, the **E5** test, which
939 is enacted when only the IR threshold is exceeded, is used
940 most often followed by the **E1** and **E4** tests. No bad data are
941 seen in this nighttime data set, probably because most cases

are due to extremely high temperatures or reflectances, which 942
do not occur at night. The day and night cloud mask test 943
statistics vary somewhat from month to month; however, the 944
results in Tables IV and V are fairly typical for both Terra 945
and Aqua. The number of positive **A** tests decreases for VIRS 946
presumably because the proportion of colder clouds drops when 947
the midlatitudes are excluded from the data set. 948

Of the pixels initially classified as clear during daytime, 949
roughly 92% are classified as good clear, 4.6% as clear glint, 950
1.6% as clear snow, 1.4% as weak clear, and the remainder 951
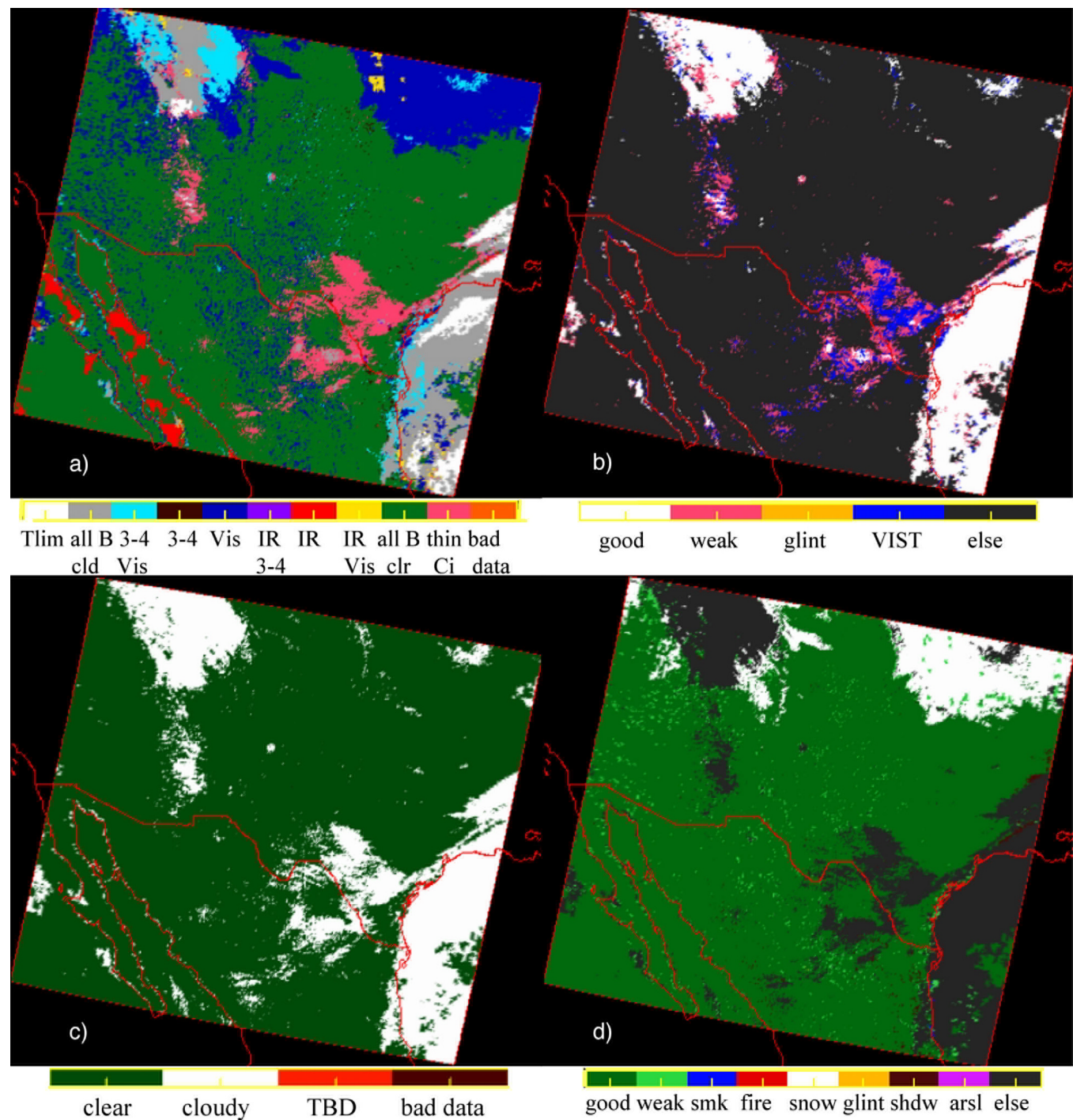
4/C   Fig. 13.   Pixel classification by CERES daytime nonpolar cloud mask for Terra MODIS image in Fig. 12(a), 1700 UTC, December 21, 2000. (a) Final tests used to classify each pixel, (b) cloud quality classification, (c) final cloud mask, and (d) final clear-sky classifications.

divided between weak clear, shadow, aerosol, and smoke. At night, approximately 80% of the pixels are good clear, 14% are weak clear, and 6% are clear snow. In daytime cloudy conditions, ~92% of the pixels are good cloud while around 3% are weak cloud, 1% are glint cloud, and 4% are classified as no retrieval. At night, roughly 98% are good clouds, 1.3% are weak clouds, and 0.5% are no retrievals, occurring mostly during twilight conditions. Roughly half of the no-retrieval pixels, which typically occur over bright surfaces like desert, snow, and glint, are reclassified as clear pixels in the retrieval

subsystem. The Terra March 2000 statistics are typical for all of the Terra and Aqua nonpolar scene classifications. The number of no retrievals from VIRS is slightly smaller, around 3%, presumably because of fewer snowy and strong sunglint conditions.

B. Cloud Amount Distributions and Consistency

The TRMM Ed2 and Terra Ed2 cloud amount distributions for March 2000 are shown in Fig. 18. This month is shown
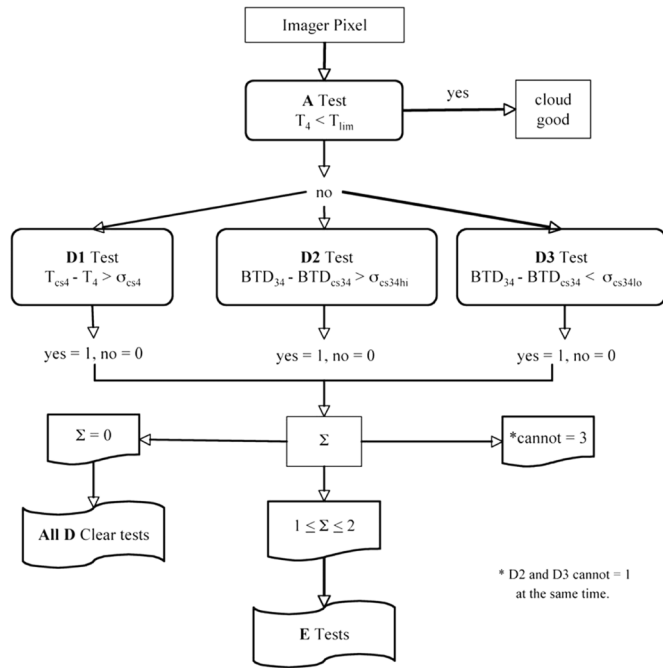
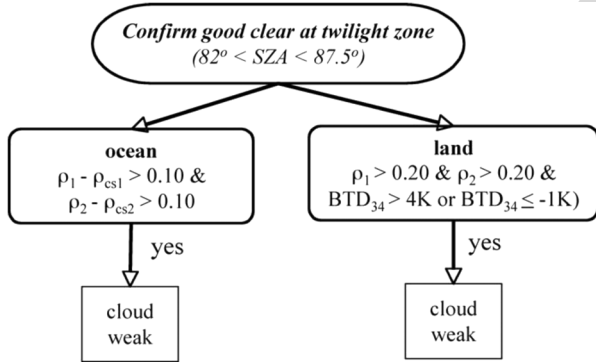Fig. 14. Schematic diagram of CERES nonpolar nighttime scene identification.

Fig. 15. Flow diagram for twilight tests applied when nighttime mask identifies pixels as good clear and significant sunlight affects the SIR brightness temperature.

970 because it is the only period when CERES broadband scan-
971 ners operated on both TRMM and Terra. The cloud amounts
972 include good, weak, and no-retrieval pixels. During daytime
973 [Fig. 18(a)], the VIRS and MODIS results have similar patterns
974 with some distinctive differences. For example, fewer clouds
975 are detected by Terra over the Sahara and most land areas,
976 whereas differences over ocean vary. Over the intertropical
977 convergence zones, the VIRS cloud amounts are greater, but
978 in the southern ocean subtropical subsidence areas, the VIRS
979 cloud cover is slightly less. These discrepancies can arise from
980 a number of factors such as differences in spectral and temporal
981 and VZA sampling characteristics. Over the Tropics, VIRS
982 samples nearly all local times during a given month, but has
983 divergent sampling patterns in the subtropics and midlatitudes.
984 On March 2000, most of the daytime samples near $32°$ N were
985 taken in the hours just before sunset and after sunrise, whereas
986 at the $32°$ S, VIRS sampled, on average, around 1300 LT.
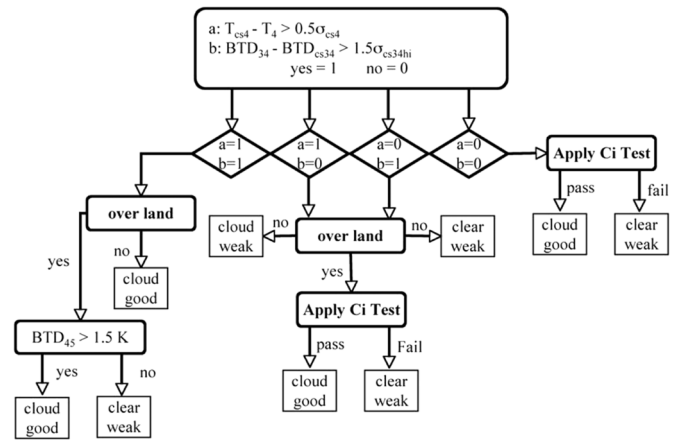987 Terra MODIS viewed a given area in the VIRS domain within

Fig. 16. Nighttime **E1** test applied when $D1 = 1$, $D2 = 1$, and $D3 = 0$.

± 1.5 h of 1030 LT at VZA $< 70°$. Thus, from a sampling stand- 988
point, many of the daytime differences are reasonable. 989

Similar sampling differences might explain the differences 990
at night [Fig. 18(b)], except over the Sahara Desert where the 991
cloud amounts from VIRS greatly exceed those from Terra. 992
In this instance, the VIRS results are likely an overestimate 993
and may be due to the use of older emissivity maps based 994
on AVHRR data [39], to differences in the surface skin tem- 995
peratures between the ECMWF and GEOS4.03 analyses, or 996
to some slight differences in the Terra Ed2 and VIRS Ed2 997
nighttime masks. Several extra twilight tests and a BTD_{64} 998
nighttime test were added for Terra Ed2. At night, the VIRS 999
analysis consistently detected many more clouds than Terra 1000
over the western Sahara during all months (not shown). The 1001
Terra processing produces an artifact, a discontinuity at $50°$ N, 1002
not seen in the VIRS, which only views to $38°$ N. It occurs 1003
because of an error in the Terra Ed2 polar mask and is discussed 1004
by Trepte *et al.* [13], [51]. 1005

Many of the latitudinal sampling inconsistencies are dimin- 1006
ished somewhat by averaging the VIRS results over periods 1007
of three months or so. Fig. 19 shows the combined cloud 1008
amounts derived from VIRS and Terra for summer 2000 (June, 1009
July, August; JJA), and winter 2000–2001 (December, January, 1010
February; DJF). During daytime [Fig. 19(a)], the VIRS zonal 1011
mean cloud amounts are systematically larger than those from 1012
Terra except south of $30°$ S. The VIRS and Terra cloud fractions 1013
are in closer agreement during the night [Fig. 19(b)] except 1014
over the northern subtropics, particularly at the latitudes ($15° -$ 1015
$32°$ N) corresponding to the Sahara Desert. It is clear that the 1016
main source of the discrepancy at those latitudes is due to 1017
the differences over land, which peak at 0.11 around $22.5°$ N 1018
[Fig. 19(c)]. Over ocean, the mean zonal differences (VIRS- 1019
MODIS) vary between -0.025 and 0.025. Overall, the zonal 1020
differences range from -0.03 to 0.05. Not all of the differences 1021
are due to changes ~~between the VIRS and Terra processing~~ 1022
in the numerical weather analyses, surface emissivities, and 1023
thresholds. The Terra orbit was selected to maximize clear- 1024
sky detection over land before land-surface heating causes the 1025
development of clouds and after early morning fog or stratus 1026
have dissipated. This fixed local-time sampling contrasts with 1027
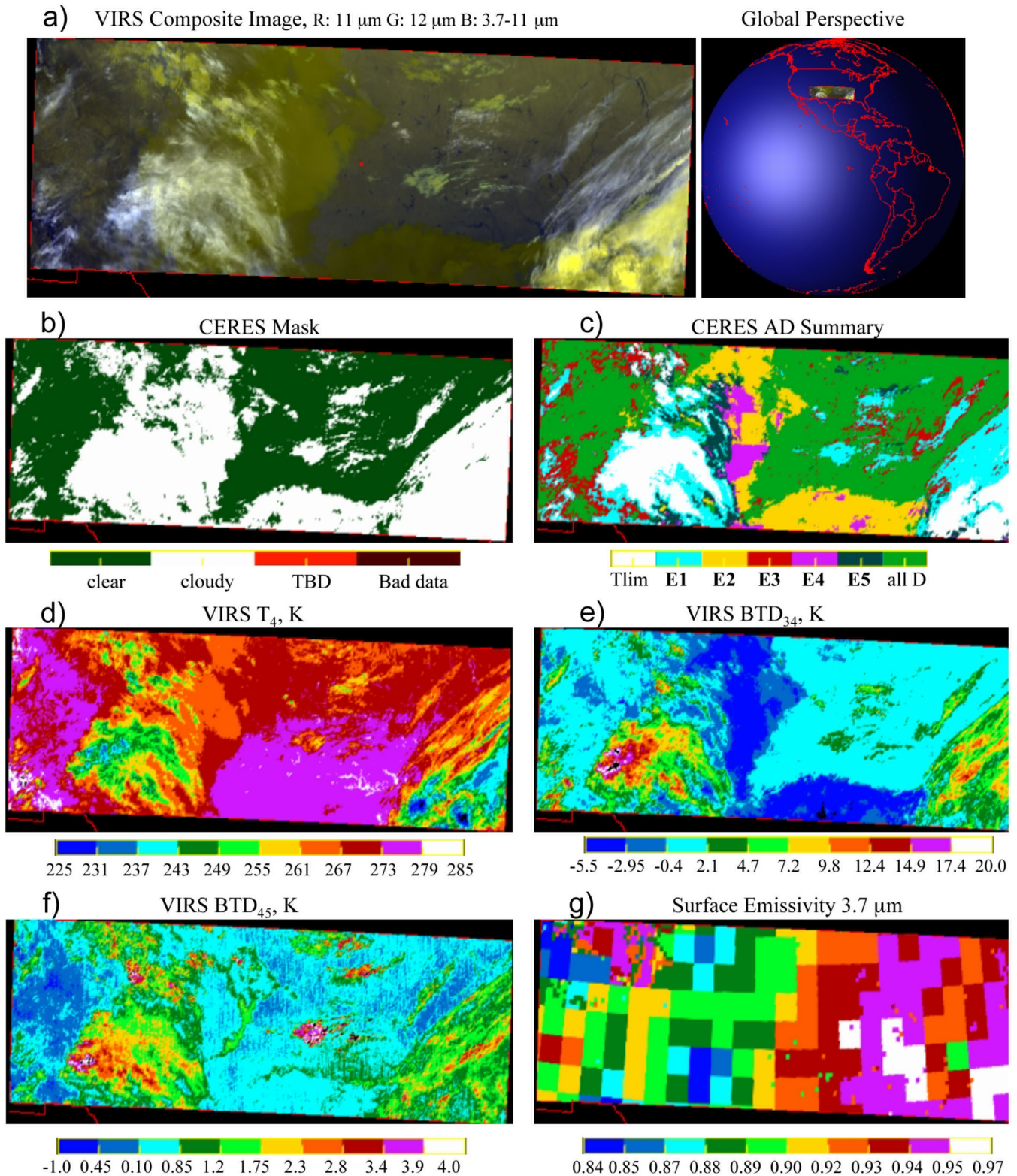the 24-h sampling by the TRMM VIRS. Thus, some of the 1028

a) VIRS Composite Image, R: 11 μm G: 12 μm B: 3.7-11 μm   Global Perspective

b) CERES Mask   c) CERES AD Summary

clear   cloudy   TBD   Bad data

Tlim   E1   E2   E3   E4   E5   all D

d) VIRS T_4, K   e) VIRS BTD_{34}, K

225 231 237 243 249 255 261 267 273 279 285

-5.5 -2.95 -0.4 2.1 4.7 7.2 9.8 12.4 14.9 17.4 20.0

f) VIRS BTD_{45}, K   g) Surface Emissivity 3.7 μm

-1.0 0.45 0.10 0.85 1.2 1.75 2.3 2.8 3.4 3.9 4.0

0.84 0.85 0.87 0.88 0.89 0.90 0.92 0.93 0.94 0.95 0.97

Fig. 17.   CERES nocturnal cloud mask for VIRS data taken at 6 UTC on March 25, 2001 over Texas.   **4/C**

differences are caused by discrepancies in the local-time sampling of the two satellites.

The relative sampling differences between Aqua and Terra are a bit easier to understand since they are both polar orbiters with fixed overpass times. The mean July 2004 daytime Aqua and Terra cloud fractions and their differences are shown in Fig. 20. A cursory examination of the means [Fig. 20(a) and (b)] indicates that they are very similar. Dissimilarities stand out better in the difference plot [Fig. 20(c)] where light green and yellow indicate good agreement, blues show that Terra has more

TABLE IV
SUMMARY OF DAYTIME CLOUD MASK TESTS USED TO REACH
FINAL CLASSIFICATION OF ALL NONPOLAR PIXELS FOR
TERRA MODIS, MARCH 2000

	Test	Ocean	Land	Desert	Total
A:	T_{lim} Cloud	0.481	0.309	0.077	0.431
All B: Clear		0.161	0.250	0.764	0.195
All B: Cloud		0.209	0.189	0.028	0.201
C1:	BTD_{34}, VIS	0.043	0.055	0.010	0.046
C2:	BTD_{34}	0.037	0.046	0.017	0.039
C3:	VIS	0.025	0.065	0.065	0.035
C4:	IR, BTD_{34}	0.013	0.022	0.020	0.015
C5:	IR	0.015	0.018	0.011	0.016
C6:	IR, VIS	0.013	0.030	0.005	0.017
	Bad Data	0.004	0.011	0.002	0.006

TABLE V
SUMMARY OF NIGHTTIME CLOUD MASK TESTS USED TO REACH
FINAL CLASSIFICATION OF ALL NONPOLAR PIXELS FOR
TERRA MODIS, MARCH 2000

	Test	Ocean	Land	Desert	Total
A:	T_{lim} Cloud	0.483	0.353	0.082	0.447
All D: Clear		0.208	0.343	0.684	0.245
E1:	IR, BTD_{34} high	0.077	0.111	0.073	0.084
E2:	BTD_{34} low	0.003	0.034	0.058	0.010
E3:	BTD_{34} high	0.005	0.043	0.052	0.014
E4:	IR, BTD_{34} low	0.067	0.036	0.006	0.060
E5:	IR	0.161	0.072	0.022	0.141
	Bad Data	0.000	0.000	0.000	0.000

cloud cover, and reds and white correspond to greater Aqua cloud amounts. Increased afternoon cloudiness is greatest over elevated land areas, some coastal lands, and over the tropical western Pacific. Greater midmorning (Terra) cloud cover is apparent over the subtropical marine stratus regions, northwest of Australia, and over the northern Amazon Basin. While the cloud cover difference is relatively small over many areas, overall for this month, it appears that cloudiness is greater around 1330 LT than at 1030 LT.

Although the differences vary from month to month, the mean 2005 cloud amounts (Fig. 21) reveal some significant systematic zonal divergences. During the daytime [Fig. 21(a)], more clouds are detected using the Aqua data over the Tropics and northern midlatitudes. Fewer clouds are seen over the southern midlatitudes. Relatively good agreement between Terra and Aqua is seen in the polar regions, except at night [Fig. 21(b)]. In other zones, the nighttime cloud cover from Aqua tends to be the same or slightly less than that from Terra. When all hours are combined [Fig. 21(c)], the differences over nonpolar ocean range between -0.03 and 0.02, with the largest differences occurring near the Equator and $40°$ S. Over land, Aqua systematically yields more clouds, by up to 6% at $12°$ S. The diurnal cycle in cloud cover over land is likely responsible for much of the Aqua–Terra bias. The large relative bias over the polar regions is primarily due to algorithm changes between Terra and Aqua [13]. Otherwise, in nonpolar regions, the CERES Terra and Aqua results are generally very consistent given their sampling differences.

C. Comparisons With Other Cloud Amounts

Fig. 22 shows the long-term zonal average cloud amounts from various sources including the ISCCP, MAST (MYD08 and MOD08), the AVHRR Pathfinder Atmospheres Extended (PATMOS-x) cloud amount data set, surface observations [52], and the three CERES data sets discussed here. The PATMOS-x data set is based on a recently updated version of the algorithm summarized by Thomas *et al.* [53]. Averages from those data sets are listed in Table VI. Although different in magnitude, the relative zonal variations are all very similar except north of $70°$ N, for all polar regions for PATMOS-x, and between $40°$ S and $70°$ S where the surface values are noisier, most likely as the result of sparse spatial sampling. In the Tropics, the PATMOS-x and MYD08 amounts are the greatest and the CERES Terra amounts are the least. The CERES values are generally closest to the historical surface averages except in the Arctic and near $20°$ N. The ISCCP amounts fall between the surface and MAST results, except in the midlatitudes where they are the largest. Overall, the CERES cloud amounts differ from the MAST and ISCCP cloud amounts by 0.07 globally and between $60°$ N and $60°$ S. The CERES cloud amounts are 0.05 and 0.07 less than the PATMOS-x cloud amounts globally and between $60°$ N and $60°$ S, respectively. The average difference between the surface and CERES cloud amounts is between 0.00 and 0.01 (Table VI).

Active sensors, including the Geoscience Laser Altimetry System (GLAS) on the Ice Cloud and Elevation Satellite and the Cloud-Aerosol Lidar and Infrared Pathfinder Satellite Observations (CALIPSO) satellite, detect even more cloud cover than any of the passive sensors. The CERES global cloud fractions are 0.00–0.08 less than those from GLAS [54] and 0.14 less than those from CALIPSO [55]. Direct comparisons with airborne [56] and surface-based lidar systems [57] revealed that the CERES algorithm fails to detect most clouds with optical depths smaller than 0.3. Very preliminary estimates from CALIPSO measurements indicate that the cloud amounts having optical depths less than 0.3 are slightly more than 0.19 [Y. Hu, 2007, personal communication]. Nearly 70% of those thin clouds detected by CALIPSO have optical depths less than 0.1. Thus, it is likely that the primary difference between the CERES and the CALIPSO and GLAS cloud retrievals is due to the inability of the CERES algorithms to detect clouds that have very low effective optical depths. These would include such clouds as thin cirrus that fills the imager pixel or small cumulus clouds that partially fill the pixel. The comparisons with the GLAS data reveal that some of the greatest differences with CERES occur in areas dominated by trade cumulus [54]. This could explain why the PATMOS-x cloud amounts, derived with most of the same channels used by CERES, are greatest in the Tropics. The updated PATMOS-x cloud mask algorithm has been tuned based on the high-resolution (250 m) MODIS pixels that can resolve many of the small clouds (A. Heidinger, 2008 personal communication). The surface-based cloud amounts may be similar in magnitude to the CERES values because surface observers may not see the very thin clouds or may discount their contribution to sky cover.

The large range in cloud cover derived from the same satellite data seen in Table VI, i.e., CERES and MAST, could be due
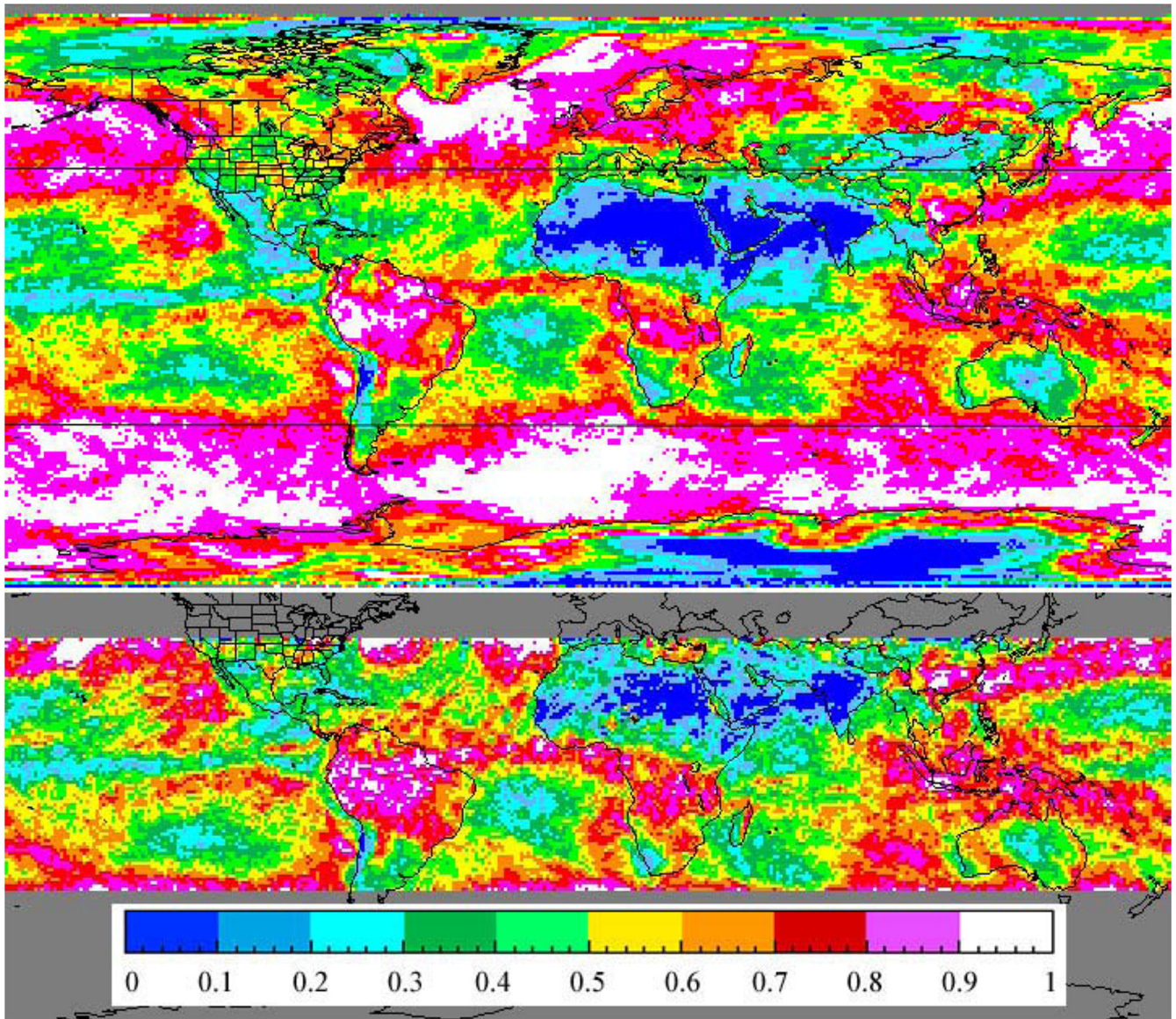
Fig. 18.   (a) Mean CERES daytime cloud amount for March 2000 from (top) Terra MODIS and (bottom) TRMM VIRS.   **4/C**

to the sensitivity of the algorithms to cloud optical thickness. This probable cause may be reflected in the relative number of cloudy pixels having no retrievals of cloud properties. When determining cloud properties, it becomes difficult to obtain a valid retrieval for very low optical depths because the errors in the input parameters often exceed the size of the cloud signal. To avoid no retrievals, the ISCCP algorithm assigns to many of those pixels a default minimum optical depth and a temperature that is 5 K less than the tropopause temperature [58]. In addition to having many thin cloud (optical depths less than 1.0) no retrievals [56], [57], the MAST Collection-5 algorithm does not attempt to retrieve cloud properties for pixels on the edges of cloud decks where the retrieval may have a large uncertainty [59].

To examine the impact of no retrievals on the cloud fraction having cloud properties, the number of pixels identified as cloudy by the MAST scene identification algorithm [6] and the number of pixels having retrieved cloud properties [8] were computed using the Collection-5 MOD06 product for daytime on July 30, 2005 to determine the fraction of no-retrieval cloudy pixels. It was found that no retrievals for the 3.7-μm retrieval—the MAST retrieval method having the greatest number of retrievals—comprise nearly 20% of the nonpolar MAST Terra cloudy pixels compared to less than 4% of those from CERES. Assuming that the single day's statistics are typical, the cloud fractions for nonpolar pixels having retrieved cloud properties are around 0.576 and 0.536 for CERES and MAST, respectively, whereas the ISCCP cloud fraction would be the same as that in Table VI because of the default value approach. Presumably, the differences between CERES and the MAST retrieved cloud fractions are due to edge pixels and optically thin clouds not retrieved by the MAST algorithms. For example, the MAST MOD06 cloud mask and retrieved optical depths are compared to their CERES counterparts in Fig. 23 for a Terra MODIS scene taken over Australia around 0100 UTC on July 30, 2005. The cloud masks are similar over ocean,
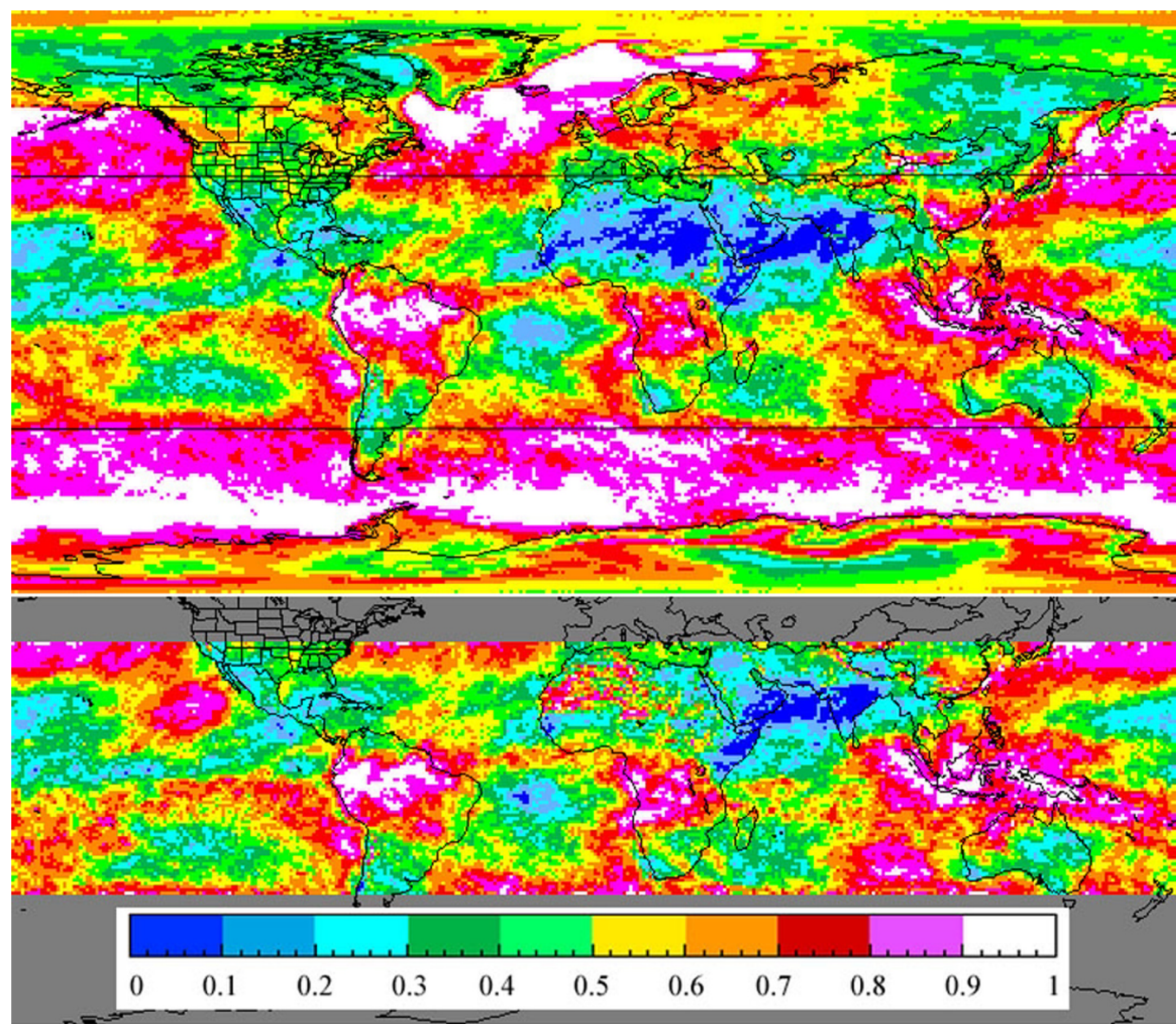
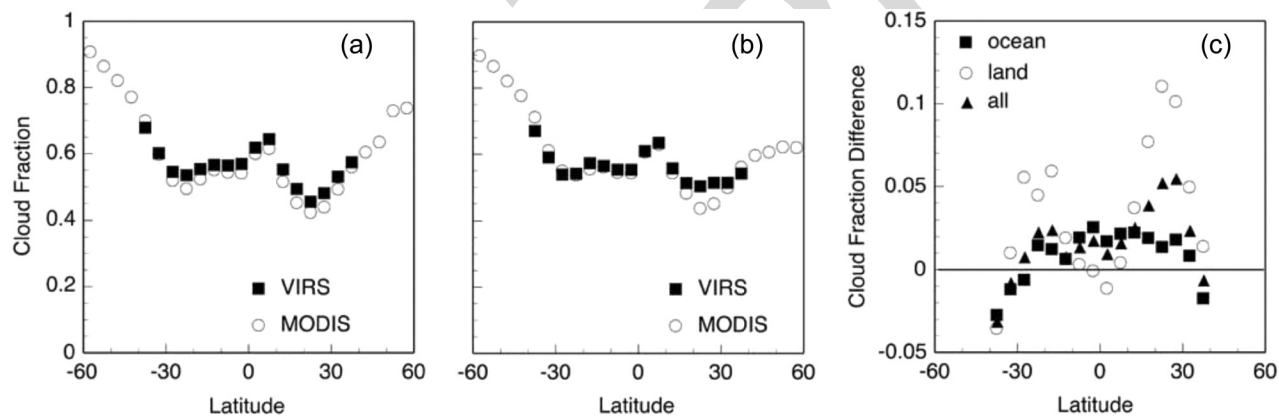Fig. 18. (*continued*). (b). Same as (a), except for nighttime. **4/C**

Fig. 19. Mean zonal cloud fraction and differences for summer 2000 (JJA) and winter 2001 (DJF). (a) Day. (b) Night. (c) 24 h.

but CERES [Fig. 23(b)] picks up a little more cloudiness than MOD06 [Fig. 23(c)] around the edges of the systems over land. The cloud cover with retrieved optical depths is further reduced for the MOD06 cases as indicated by the areas with optical depth retrievals [Fig. 23(e)]. This is particularly notice-able over water where smaller clouds disappear and the clear
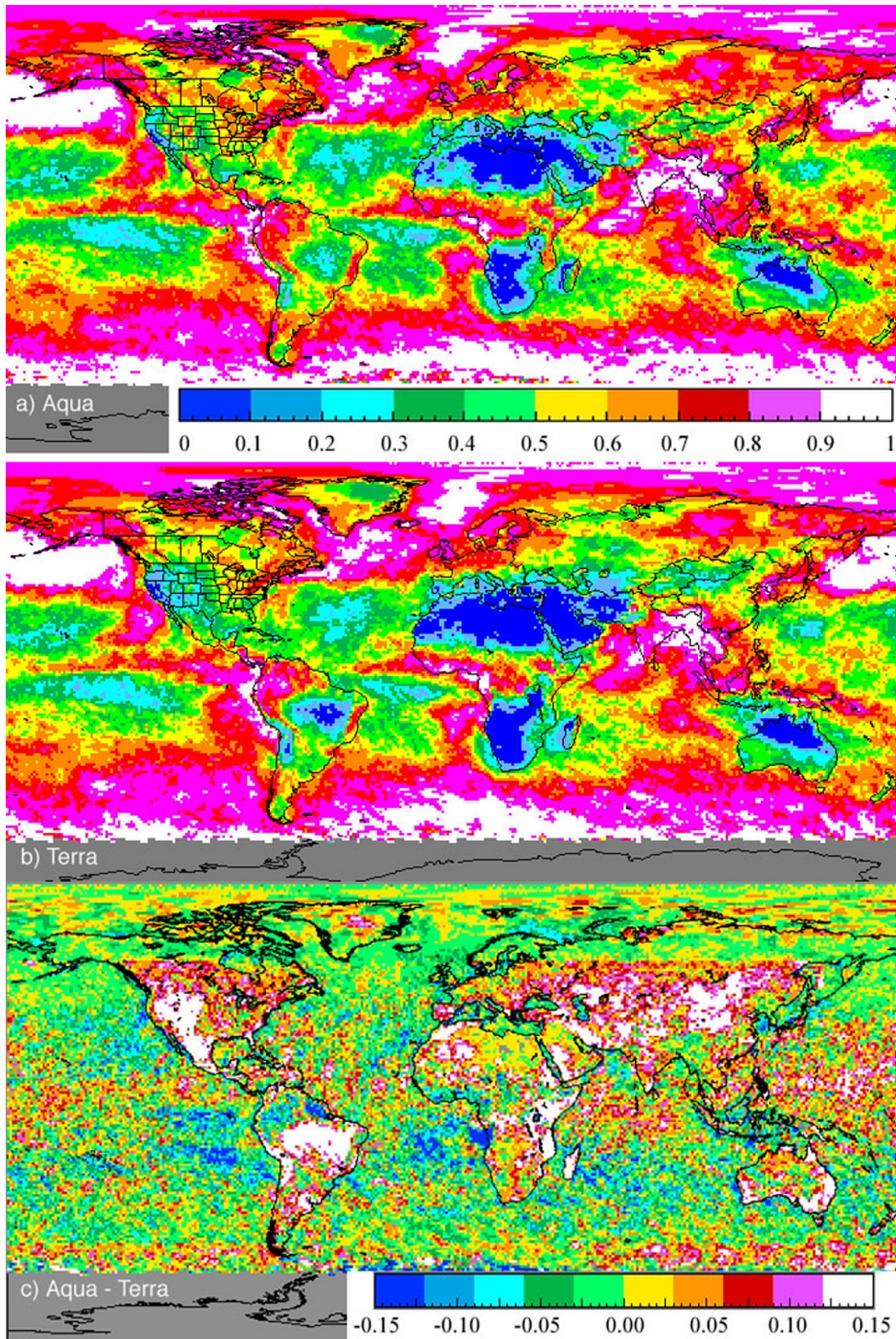
Fig. 20. Mean cloud fraction distributions and differences for July 2004.   **4/C**

1166 areas along the cloud edges are increased. In most instances,
1167 these removed pixels correspond to clouds identified as having
1168 small optical depths (less than one) by CERES [Fig. 23(d)].
1169 Since most of the clouds missed by CERES are very thin

optically, they should have minimal impact on the radiation 1170
field. If they were detected, it appears that it would be very 1171
difficult to retrieve the corresponding cloud properties with 1172
much certainty. Nevertheless, to fully account for the impact of 1173
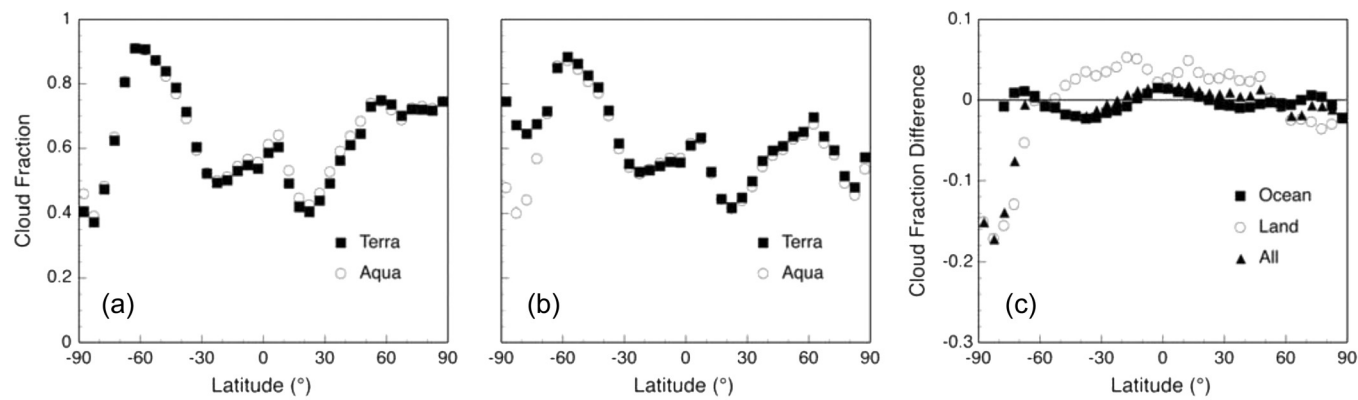
Fig. 21. Mean 2005 CERES zonal cloud fraction and difference. (a) Day. (b) Night. (c) All hours.
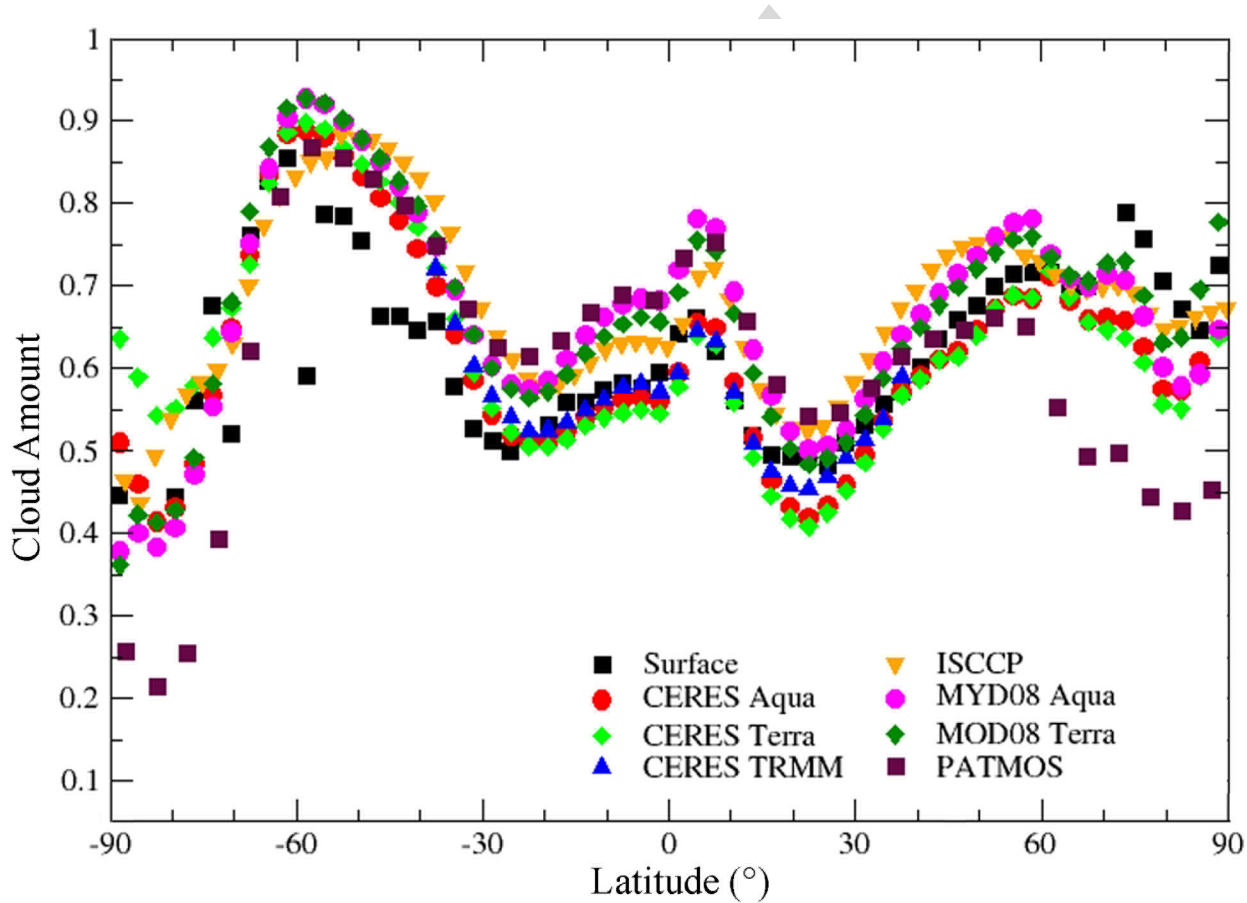

Fig. 22. Mean long-term zonal cloud amounts from several sources. The time periods and averages are listed in Table VI. **4/C**

TABLE VI
MEAN CLOUD AMOUNTS FROM LONG-TERM MEASUREMENTS

Source	Time Period	Global	60°S –60°N	37.5°S – 37.5°N
Surface	1971-1996	0.601	0.590	0.554
ISCCP	1983-2001	0.675	0.673	0.621
PATMOS-x	1981-2006	0.651	0.671	0.644
MOD08 *Terra*	2000-2005	0.668	0.662	0.614
MYD08 *Aqua*	2002-2005	0.678	0.677	0.632
CERES *Terra*	2000-2005	0.602	0.597	0.543
CERES *Aqua*	2002-2005	0.604	0.595	0.543
CERES VIRS	1998-2000	N/A	N/A	0.554

all clouds, it would be necessary to make such retrievals or to estimate their properties in some fashion, e.g., as in the ISCCP algorithm.

Other factors that affect cloud detectability include very high solar zenith angles (i.e., the twilight zone) and aerosols. When the aerosol optical depth is very large, as sometimes occurs during dust storms, the CERES nonpolar algorithm often misclassifies the heavy aerosol areas as cloudy. Because dust aerosols often produce multispectral radiance combinations that do not fit the model-computed radiances for clouds, some of those pixels end up as no retrievals while
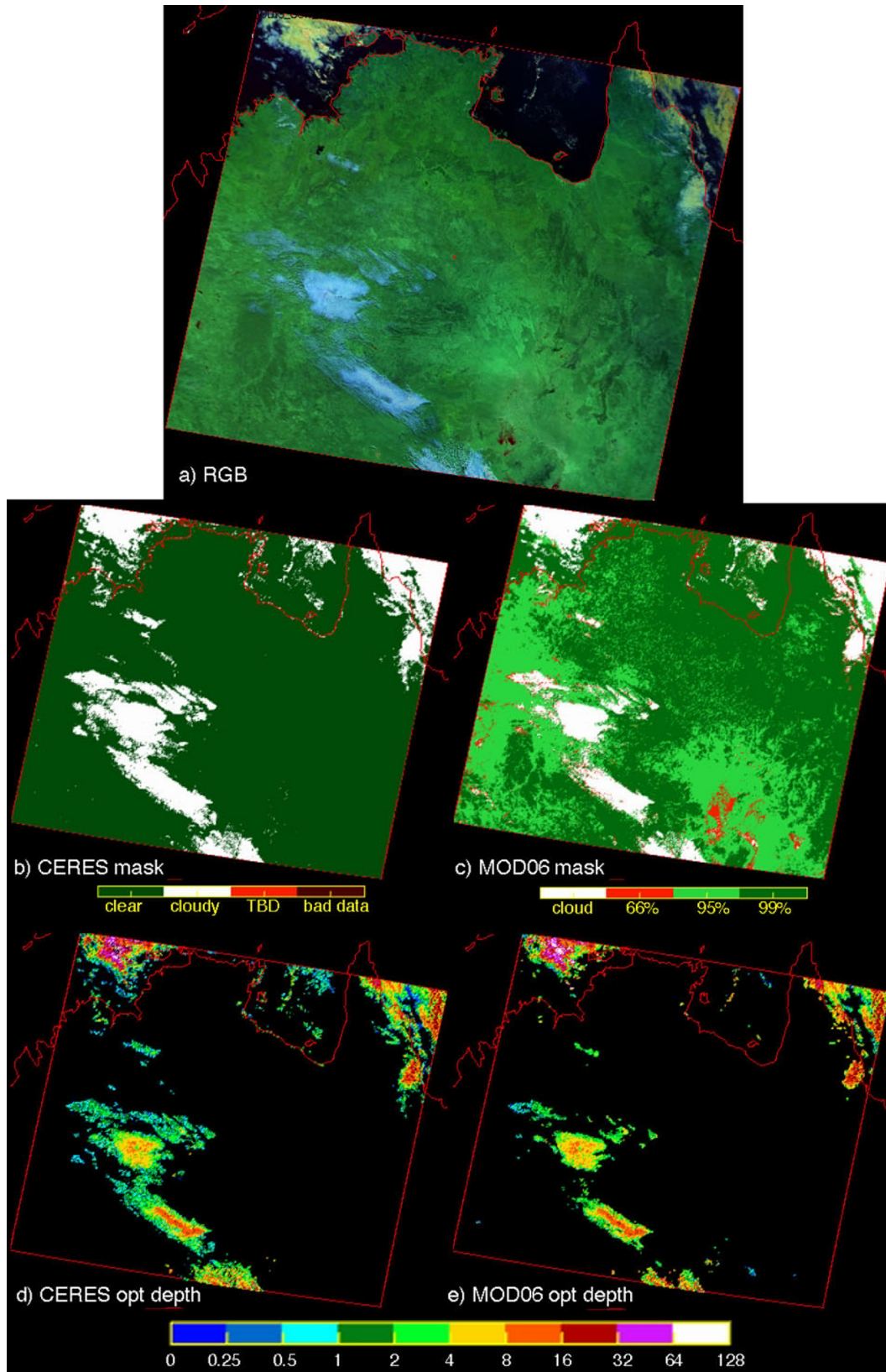
Fig. 23.   Image, cloud mask, and cloud optical depths. Numbers in (c) denote probability of being clear. From Terra MODIS, 0100 UTC, July 30, 2005.   **4/C**

others have abnormal cloud properties, a topic discussed in [14] and [47]. The net impact of misclassified aerosols is a slight increase in cloud cover. In the twilight near-terminator zone, initial comparisons with CALIPSO data indicate that the loss of the BTD_{34} signal for low clouds causes a slight net decrease in the cloud cover. Accurate quantification of the impacts of heavy aerosol loading and the poor BTD_{34} signal in near-terminator conditions will require detailed analyses of

coincident imager and active sensor lidar data (e.g., CALIPSO). Such analyses would help define the optical depth thresholds where aerosols are misclassified as clouds and provide the basis for improving cloud detection in dusty and twilight conditions.

V. CONCLUDING REMARKS

A multispectral algorithm has been developed for CERES to discriminate clouds from cloud-free scenes in nonpolar regions primarily using channels common to both VIRS and MODIS to maintain some consistency across platforms. It has already been applied to many years of VIRS and MODIS data. Although it produces cloud amounts that are up to 10% less than those determined from other techniques and satellite data, the methodology appears to be quite successful at consistently detecting most clouds that are of radiative significance and correspond to those seen from the surface. Further validation and error assessment studies are needed to fully quantify the impact of any undetected clouds.

Through cross-calibration, it was found that several of the channels common to VIRS, Terra MODIS, and Aqua MODIS are inconsistent. The VIS channel calibration differences have been discussed elsewhere [19]. The radiances measured by the 1.6-μm channel on the VIRS are too low by 19% compared to the corresponding Terra MODIS channel and were increased by 17%, on basis of earlier analyses, for use in the VIRS Ed2 processing. The Terra 3.8-μm channel also shows some significant differences compared with the same channel on Aqua. It is important that users of the MODIS data recognize these discrepancies. Future editions of the CERES algorithms will take them into account during processing.

Given that CERES was short-lived on TRMM and the 1.6-μm channel failed on Aqua MODIS, the cross-platform consistency requirement between the VIRS and MODIS masks is no longer critical except between Aqua and Terra MODIS. Thus, in the future, additional channels from the MODIS, such as the CO_2-absorption channels and the high-resolution VIS channel, could be used to improve the detection of small cumulus and thin cirrus that are currently missed using the software editions described here. Other channels could also be used to improve separation of aerosols and clouds, and other high-resolution ancillary data sets, such as spectral surface albedos [37], [38] and emissivities [42] from the MODIS land surface properties teams, might be useful for refining the cloud detection in low-contrast conditions.

Because it relies on channels that are used on many operational meteorological satellites, the current CERES nonpolar mask has already been adapted for use with several of those satellites (see, e.g., [60]). Combined with the CERES polar mask [13], [51] and cloud property retrieval [14], [47] algorithms and the CERES scanner radiances, it has produced numerous valuable data products covering much of the past decade. Those products have already advanced our understanding of the radiative impact of clouds (see, e.g., [2] and [61]) and their interaction with the climate system (see, e.g., [62] and [63]). They have the potential for many other uses in the future.

REFERENCES

[1] B. A. Wielicki *et al.*, "Clouds and the Earth's Radiant Energy System (CERES): Algorithm overview," *IEEE Trans. Geosci. Remote Sens.*, vol. 36, no. 4, pp. 1127–1141, Jul. 1998.

[2] N. G. Loeb, N. Manalo-Smith, S. Kato, W. F. Miller, S. Gupta, P. Minnis, and B. A. Wielicki, "Angular distribution models for top-of-atmosphere radiative flux estimation from the Clouds and the Earth's Radiant Energy System instrument on the Tropical Rainfall Measuring Mission satellite. Part I: Methodology," *J. Appl. Meteorol.*, vol. 42, no. 2, pp. 240–265, 2003.

[3] B. A. Wielicki, R. D. Cess, M. D. King, D. A. Randall, and E. F. Harrison, "Mission to planet Earth: Role of clouds and radiation in climate," *Bull. Amer. Meteorol. Soc.*, vol. 76, no. 11, pp. 2125–2153, Nov. 1995.

[4] B. A. Wielicki, B. R. Barkstrom, E. F. Harrison, R. B. Lee, III, G. L. Smith, and J. E. Cooper, "Clouds and the Earth's Radiant Energy System (CERES): An Earth observing system experiment," *Bull. Amer. Meteorol. Soc.*, vol. 77, no. 5, pp. 853–867, May 1996.

[5] W. B. Rossow and R. A. Schiffer, "Advances in understanding clouds from ISCCP," *Bull. Amer. Meteorol. Soc.*, vol. 80, no. 11, pp. 2261–2287, Nov. 1999.

[6] S. A. Ackerman, K. I. Strabala, W. P. Menzel, R. A. Frey, C. C. Moeller, and L. E. Gumley, "Discriminating clear sky from clouds with MODIS," *J. Geophys. Res.*, vol. 103, no. D24, pp. 32 141–32 157, 1998.

[7] M. D. King *et al.*, "Cloud and aerosol properties, precipitable water, and profiles of temperature and water vapor from MODIS," *IEEE Trans. Geosci. Remote Sens.*, vol. 41, no. 2, pp. 442–458, Feb. 2003.

[8] S. Platnick, M. D. King, S. A. Ackerman, W. P. Menzel, B. A. Baum, J. C. Riedl, and R. A. Frey, "The MODIS cloud products: Algorithms and examples from Terra," *IEEE Trans. Geosci. Remote Sens.*, vol. 41, no. 2, pp. 459–473, Feb. 2003.

[9] D. F. Young, P. Minnis, G. G. Gibson, D. R. Doelling, and T. Wong, "Temporal interpolation methods for the Clouds and the Earth's Radiant Energy System (CERES) experiment," *J. Appl. Meteorol.*, vol. 37, no. 6, pp. 572–590, Jun. 1998.

[10] L. Gomez-Chova, G. Camps-Valls, J. Calpe-Maravilla, L. Guanter, and J. Moreno, "Cloud-screening algorithm for ENVISAT/MERIS multispectral images," *IEEE Trans. Geosci. Remote Sens.*, vol. 45, no. 12, pp. 4105–4118, Dec. 2007.

[11] J. V. Martins, D. Tanre, L. A. Remer, Y. J. Kaufman, S. Mattoo, and R. Levy, "MODIS cloud screening for remote sensing of aerosols over oceans using spatial variability," *Geophys. Res. Lett.*, vol. 29, no. 12, p. 8009, 2002. DOI:1029/2001GL013252.

[12] M. Wang and W. Shi, "Cloud masking for ocean color data processing in the coastal regions," *IEEE Trans. Geosci. Remote Sens.*, vol. 44, no. 11, pp. 3196–3205, Nov. 2006.

[13] Q. Trepte, P. Minnis, D. A. Spangenberg, R. F. Arduini, S. Sun-Mack, and Y. Chen, "Polar cloud and snow discrimination for CERES using MODIS data," *IEEE Trans. Geosci. Remote Sens.*, 2008. submitted for publication.

[14] P. Minnis, S. Sun-Mack, D. F. Young, P. W. Heck, D. P. Garber, Y. Chen, D. A. Spangenberg, B. A. Wielicki, and E. B. Geier, "Cloud property retrievals for CERES using TRMM VIRS and Terra and Aqua MODIS data," *IEEE Trans. Geosci. Remote Sens.*, 2008. submitted for publication.

[15] S. Sun-Mack, P. Minnis, Y. Chen, R. F. Arduini, and D. F. Young, "Visible clear-sky and near-infrared surface albedos derived from VIRS and MODIS data for CERES," *IEEE Trans. Geosci. Remote Sens.*, 2008. submitted for publication.

[16] C. Kummerow, W. Barnes, T. Kozu, J. Shine, and J. Simpson, "The Tropical Rainfall Measuring Mission (TRMM) sensor package," *J. Atmos. Ocean. Technol.*, vol. 15, no. 3, pp. 809–817, Jun. 1998.

[17] P. Minnis, L. Nguyen, D. R. Doelling, D. F. Young, W. F. Miller, and D. P. Kratz, "Rapid calibration of operational and research meteorological satellite imagers. Part I: Evaluation of research satellite visible channels as references," *J. Atmos. Ocean. Technol.*, vol. 19, no. 9, pp. 1233–1249, Sep. 2002.

[18] P. Minnis, L. Nguyen, D. R. Doelling, D. F. Young, W. F. Miller, and D. P. Kratz, "Rapid calibration of operational and research meteorological

satellite imagers. Part II: Comparison of infrared channels," *J. Atmos. Ocean. Technol.*, vol. 19, no. 9, pp. 1250–1266, Sep. 2002.

[19] P. Minnis, D. R. Doelling, L. Nguyen, W. F. Miller, and V. Chakrapani, "Assessment of the visible channel calibrations of the VIRS on TRMM and MODIS on Aqua and Terra," *J. Atmos. Ocean. Technol.*, vol. 25, no. 3, pp. 385–400, Mar. 2008.

[20] A. Ignatov, "Spurious signals in TRMM/VIRS reflectance channels and their effect on aerosol retrievals," *J. Atmos. Ocean. Technol.*, vol. 20, no. 8, pp. 1120–1137, Aug. 2003.

[21] A. Ignatov and L. L. Stowe, "Physical basis, premises, and self-consistency checks of aerosol retrievals from TRMM VIRS," *J. Appl. Meteorol.*, vol. 39, no. 12, pp. 2259–2277, Dec. 2000.

[22] C. H. Lyu, R. A. Barnes, and W. L. Barnes, "First results from the on-orbit calibrations of the Visible and Infrared Scanner for the Tropical Rainfall Measuring Mission," *J. Atmos. Ocean. Technol.*, vol. 17, no. 4, pp. 385–394, Apr. 2000.

[23] C.-H. Lyu and W. L. Barnes, "Four years of TRMM/VIRS on-orbit calibrations and characterization using lunar models and data from Terra/MODIS," *J. Atmos. Ocean. Technol.*, vol. 20, no. 3, pp. 333–347, Mar. 2003.

[24] D. F. Young, P. Minnis, and R. F. Arduini, "A comparison of cloud microphysical properties derived using VIRS 3.7 and 1.6 μm data," in *Proc. AMS 10th Conf. Atmos. Radiat.*, Madison, WI, Jun. 28–Jul. 2 1999, pp. 25–28.

[25] W. L. Barnes, T. S. Pagano, and V. V. Salomonson, "Prelaunch characteristics of the Moderate Resolution Imaging Spectroradiometer (MODIS) on EOS-AM1," *IEEE Trans. Geosci. Remote Sens.*, vol. 36, no. 4, pp. 1088–1100, Jul. 1998.

[26] S.-K. Yang, S. Zhou, and A. J. Miller, *SMOBA: A 3-Dimensional Daily Ozone Analysis Using SBUV/2 and TOVS Measurements*, 2006. [Online]. Available: http://www.cpc.ncep.noaa.gov/products/stratosphere/SMOBA/smoba_doc.shtml

[27] S. Bloom, A. da Silva, D. Dee, M. Bosilovich, J.-D. Chern, S. Pawson, S. Schubert, M. Sienkiewicz, I. Stajner, W.-W. Tan, and M.-L. Wu, "Documentation and validation of the Goddard Earth Observing System (GEOS) data assimilation system—Version 4," NASA Goddard Space Flight Center, Greenbelt, MD, Tech. Rep. Series on Global Modeling and Data Assimilation 104606, 2005. 165 pp.

[28] S. K. Gupta, N. A. Ritchey, F. G. Rose, T. L. Alberta, T. P. Charlock, and L. H. Coleman, "Regrid humidity and temperature fields (system 12.0)," in "CERES Algorithm Theoretical Basis Document Release 2.2," NASA Langley Res. Center, Hampton, VA, NASA/RP-1376, 1997. 20 pp. [Online]. Available: http://asd-www.larc.nasa.gov/ATBD/ATBD.html

[29] A. Nolin, R. L. Armstrong, and J. Maslanik, *Near Real-Time SSM/I EASE-Grid Daily Global Ice Concentration and Snow Extent, January to March 2004*, Boulder, CO: Nat. Snow Ice Data Center. Updated daily 1998. [Online]. Available: http://nsidc.org/data/docs/daac/nise1_nise.gd.html

[30] B. H. Ramsay, "The interactive multisensor snow and ice mapping system," *Hydrol. Processs.*, vol. 12, no. 10/11, pp. 1537–1546, 1998.

[31] S. Sun-Mack, Y. Chen, T. D. Murray, P. Minnis, and D. F. Young, "Visible clear-sky and near-infrared surface albedos derived from VIRS for CERES," in *Proc. AMS 10th Conf. Atmos. Radiat.*, Madison, WI, Jun. 28–Jul. 2 1999, pp. 422–425.

[32] Y. Chen, S. Sun-Mack, P. Minnis, and R. F. Arduini, "Clear-sky narrowband albedo variations derived from VIRS and MODIS data," in *Proc. AMS 12th Conf. Atmos. Radiat.*, Madison, WI, Jul. 10–14, 2006. CD-ROM, 5.6.

[33] A. S. Belward, J. E. Estes, and K. D. Kline, "The IGBP-DIS global 1-km land-cover data set DISCover: A project overview," *Photogramm. Eng. Remote Sens.*, vol. 65, no. 9, pp. 1013–1020, Sep. 1999.

[34] P. Minnis and E. F. Harrison, "Diurnal variability of regional cloud and clear-sky radiative parameters derived from GOES data. Part I: Analysis method," *J. Clim. Appl. Meteorol.*, vol. 23, no. 7, pp. 993–1011, Jul. 1984.

[35] J. T. Suttles, R. N. Green, P. Minnis, G. L. Smith, W. F. Staylor, B. A. Wielicki, I. Walker, D. F. Young, V. R. Taylor, and L. L. Stowe, "Angular radiation models for Earth-atmosphere system," NASA Langley Res. Center, Hampton, VA, Shortwave Radiation, NASA/RP-1184, 1988. 144 pp.

[36] K. T. Kriebel, "Measured spectral bidirectional reflection properties of four vegetated surfaces," *Appl. Opt.*, vol. 17, no. 2, pp. 253–259, Jan. 1978.

[37] E. G. Moody, M. D. King, S. Platnick, C. B. Schaaf, and F. Gao, "Spatially complete global spectral surface albedos: Value-added datasets derived from Terra MODIS land products," *IEEE Trans. Geosci. Remote Sens.*, vol. 43, no. 1, pp. 144–158, Jan. 2005.

[38] E. G. Moody, M. D. King, C. B. Schaaf, and D. K. Hall, "Northern Hemisphere five-year average (2000–2004) spectral albedos of sur-

faces in the presence of snow: Statistics computed from Terra MODIS land products," *Remote Sens. Environ.*, vol. 111, no. 2/3, pp. 337–345, Nov. 2007.

[39] Y. Chen, S. Sun-Mack, P. Minnis, D. F. Young, and W. L. Smith, Jr., "Surface emissivity derived for infrared remote sensing from satellites," in *Proc. AMS 11th Conf. Satellite Meteorol. Oceanography*, Madison, WI Oct. 15–18, 2001, pp. 512–515.

[40] Y. Chen, S. Sun-Mack, P. Minnis, D. F. Young, and W. L. Smith, Jr., "Seasonal surface spectral emissivity derived from Terra MODIS data," in *Proc. 13th AMS Conf. Satellite Oceanogr. Meteorol.*, Norfolk, VA, Sep. 20–24, 2004. CD-ROM, P2.4.

[41] Z. Wan and Z.-L. Li, "A physics-based algorithm for retrieving land-surface emissivity and temperature from EOS/MODIS data," *IEEE Trans. Geosci. Remote Sens.*, vol. 35, no. 4, pp. 980–996, Jul. 1997.

[42] S. W. Seemann, E. E. Borbas, R. O. Knuteson, G. R. Stephenson, and H.-L. Huang, "Development of a global infrared land surface emissivity database for application to clear sky sounding retrievals from multispectral satellite radiance measurements," *J. Appl. Meteorol. Climatol.*, vol. 47, no. 1, pp. 108–123, 2008.

[43] I. F. Trigo, L. F. Peres, C. C. DaCamara, and S. C. Freitas, "Thermal land surface emissivity retrieved from SEVIRI/Meteosat," *IEEE Trans. Geosci. Remote Sens.*, vol. 46, no. 2, pp. 307–314, Feb. 2008.

[44] D. P. Kratz, "The correlated k-distribution technique as applied to the AVHRR channels," *J. Quant. Spectrosc. Radiat. Transf.*, vol. 53, no. 5, pp. 501–517, May 1995.

[45] F. Rose, T. P. Charlock, D. A. Rutan, and G. L. Smith, "Tests of a constraint algorithm for the surface and atmospheric radiation budget," in *Proc. AMS 9th Conf. Atmos. Radiat.*, Long Beach, CA, Feb. 2–7, 1997, pp. 466–469.

[46] B. Baum, R. M. Welch, P. Minnis, L. L. Stowe, J. A. Coakley, Jr., J. Titlow, V. Tovinkere, P. W. Heck, Q. Trepte, D. R. Doelling, S. Mayor, T. Berendes, Q. Han, S. A. Christopher, K.-S. Kuo, M. Penaloza, A. Logar, and P. Davis, "Imager clear-sky determination and cloud detection (Subsystem 4.1). Clouds and the Earth's Radiant Energy System (CERES) algorithm theoretical basis document," NASA, Washington DC, pp. 43–82, Cloud Analyses and Radiance Inversions (Subsystem 4), NASA/RP-1376, 1995.

[47] P. Minnis, "Cloud optical property retrieval (Subsystem 4.3) Clouds and the Earth's Radiant Energy System (CERES) algorithm theoretical basis document," NASA, Washington DC, pp. 135–176, Cloud Analyses and Radiance Inversions (Subsystem 4), NASA/RP-1376, 1995. edited by CERES Sciene Team.

[48] R. M. Welch, S. K. Sengupta, A. K. Goroch, R. Palikonda, N. Rangaraj, and M. S. Navar, "Polar cloud and surface classification using AVHRR imagery—An intercomparison of methods," *J. Appl. Meteorol.*, vol. 31, no. 5, pp. 405–420, May 1992.

[49] P. Minnis, D. P. Garber, D. F. Young, R. F. Arduini, and Y. Takano, "Parameterizations of reflectance and effective emittance for satellite remote sensing of cloud properties," *J. Atmos. Sci.*, vol. 55, no. 22, pp. 3313–3339, Nov. 1998.

[50] R. W. Saunders and K. T. Kriebel, "An improved method for detecting clear sky and cloudy radiances from AVHRR data," *Int. J. Remote Sens.*, vol. 9, no. 1, pp. 123–150, Jan. 1988.

[51] Q. Trepte, P. Minnis, and R. F. Arduini, "Daytime and nighttime polar cloud and snow identification using MODIS data," in *Proc. SPIE—3rd Int. Asia-Pacific Environ. Remote Sensing Symp.*, Hangzhou, China, Oct. 23–27, 2002, vol. 4891, pp. 449–459.

[52] C. J. Hahn and S. G., "Extended edited synoptic cloud reports from ships and land stations over the globe, 1952–1996". Oak Ridge, TN: Carbon Dioxide Inf. Anal. Center, Oak Ridge Nat. Lab., 1999. NDP026C, 80 pp.

[53] S. M. Thomas, A. K. Heidinger, and M. J. Pavolonis, "Comparison of NOAA's operational AVHRR-derived cloud amount to other satellite-derived cloud climatologies," *J. Clim.*, vol. 17, no. 24, pp. 4805–4822, 2004.

[54] P. Minnis, S. Sun-Mack, Y. Chen, Q. Z. Trepte, and Y. Yi, "Comparison of CERES-MODIS and IceSat GLAS cloud amounts," *J. Geophys. Res.*, 2008. submitted for publication.

[55] S. Sun-Mack, B. A. Wielicki, P. Minnis, S. Gibson, and Y. Chen, "Integrated cloud-aerosol-radiation product using CERES, MODIS, CALIPSO, and CloudSat data," in *Proc. SPIE Europe—Conf. Remote Sens. Clouds Atmos.*, Florence, Italy, Sep. 17–19, 2007, vol. 6745.

[56] M. Chiriaco, H. Chepfer, P. Minnis, M. Haeffelin, S. Platnick, D. Baumgardner, P. Dubuisson, M. McGill, V. Noel, J. Pelon, D. Spangenberg, S. Sun-Mack, and G. Wind, "Comparison of CALIPSO-like, LaRC, and MODIS retrievals of ice cloud properties over SIRTA in France and Florida during CRYSTAL-FACE," *J. Appl. Meteorol. Climatol.*, vol. 46, pp. 249–272, 2007.

[57] G. G. Mace, Y. Zhang, S. Platnick, M. D. King, P. Minnis, and P. Yang, "Evaluation of cirrus cloud properties from MODIS radiances using cloud properties derived from ground-based data collected at the ARM SGP site," *J. Appl. Meteorol.*, vol. 44, pp. 221–240, 2005.

[58] W. B. Rossow, A. W. Walker, D. E. Beuschel, and M. D. Roiter, "International Satellite Cloud Climatology Project (ISCCP) documentation of new cloud datasets," World Meteorol. Org., Geneva, Switzerland, WMO/TD-No. 737, 1996. 115 pp.

[59] S. Platnick and M. D. King, "Update on the MODIS Collection 5 processing cloud optical depth and microphysical algorithm and product validation," in *Proc. OSA FTS/HISE Top. Meeting Tabletop Exhibit*, Santa Fe, NM, Feb. 12–15, 2007. CD-ROM, HTuA1.

[60] P. Minnis, W. L. Smith, Jr., L. Nguyen, D. A. Spangenberg, P. W. Heck, R. Palikonda, J. K. Ayers, C. Wolff, and J. J. Murray, "Near-real time cloud properties and aircraft icing indices from GEO and LEO satellites," in *Proc. SPIE—49th Annu. Meeting., Weather Environ. Satellites Conf.*, Denver, CO, Aug. 2–3, 2004, vol. 5549, pp. 145–155.

[61] B. A. Wielicki, T. M. Wong, R. P. Allan, A. Slingo, J. T. Kiehl, B. J. Soden, C. T. Gordon, A. J. Miller, S. K. Yang, D. A. Randall, F. Robertson, J. Susskind, and H. Jacobowitz, "Evidence for large decadal variability in the tropical mean radiative energy budget," *Science*, vol. 295, no. 5556, pp. 841–844, Feb. 2002.

[62] B. A. Wielicki, T. Wong, N. Loeb, P. Minnis, K. Priestley, and R. Kandel, "Changes in Earth's albedo measured by satellite," *Science*, vol. 308, no. 5723, p. 825, May 2005.

[63] S. Kato, N. G. Loeb, P. Minnis, J. A. Francis, T. P. Charlock, D. Rutan, E. E. Clouthiaux, and S. Sun-Mack, "Seasonal and interannual variations of top-of-atmosphere irradiance and cloud cover over polar regions derived from the CERES data set," *Geophys. Res. Lett.*, vol. 33, p. L19 804, 2005. DOI:10.1029/2006GL026685.

Patrick Minnis received the B.E. degree in materials science and metallurgical engineering from Vanderbilt University, Nashville, TN, in 1972, the M.S. degree in atmospheric science from Colorado State University, Fort Collins, in 1978, and the Ph.D. degree in meteorology from the University of Utah, Salt Lake City, in 1991.

He is currently a Senior Research Scientist with the Climate Science Branch, Science Directorate, NASA Langley Research Center, Hampton, VA, where he has served for more than 27 years. He is a member of the CERES, ARM, CALIPSO, and ICESat ScienceTeams and leads a research group conducting analyses of polar-orbiting and geostationary satellite data for field missions, operational aircraft icing condition diagnosis, and contrail research. He is the Author/Coauthor of over 170 peer-reviewed publications. He is currently an Editor for the *Journal of Atmospheric Sciences*. His research is focused on the remote sensing of clouds and surface properties from satellite imagery for weather and climate investigations.

Dr. Minnis was the recipient of the NASA medals for Exceptional Scientific Achievement in 1993, Exceptional Achievement in 2005, and Exceptional Service in 2008. He received the AMS Henry G. Houghton Award for Atmospheric Physics in 1998.
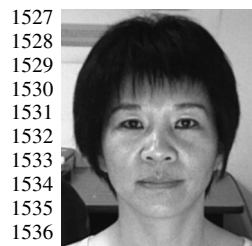
Qing Z. Trepte received the B.S. degree in atmospheric physics from Nanjing University, Nanjing, China, in 1983, and the M.S. degree in meteorology from the University of Wisconsin–Madison, Madison, in 1990.

She is currently an Atmospheric Scientist with Science Systems and Applications, Inc., Hampton, VA, and is a member of the NASA Langley CERES cloud retrieval team. She has primary responsibility for developing, testing, and validating algorithm improvements to the daytime, nighttime, and twilight CERES cloud masks for polar and nonpolar regions using MODIS, GOES, MSG, and MTSAT satellite data.
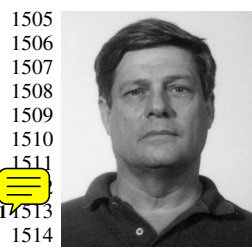
Szedung (Sunny) Sun-Mack received the B.S. degree in astrophysics from Peking University, Beijing, China, the M.S. degree in physics from the University of Maryland, College Park, and the Ph.D. degree in physics from Simon Fraser University/ Tri-Universities Meson Facility (TRIUMF), Vancouver, BC, Canada, in 1994.

She was with the CERES working team, National Aeronautics and Space Administration (NASA) Langley Research Center (LaRC), Hampton, VA, through various contract companies (Lockheed, SAIC, and SSAI), in 1993, and has worked on many projects like A-Train and NPP as well as CERES from 1995 to 2008. Prior to that, she held a research position with TRIUMF, Canada's National Laboratory for Particle and Nuclear Physics, for three years and with Beijing Astronomical Observatory, China Academia Sinica, for two years. She is currently with Science Systems and Applications, Inc., Hampton. Her research experience includes cloud and surface remote sensing, validation, integration of cloud properties from MODIS, CALIPSO, and CloudSat, and developing and operating large complex end-to-end processing systems.

Yan Chen received the B.S. degree in mechanical engineering from Shanghai Jiao Tong University, Shanghai, China, in 1984, and the M.S. degree in mechanical engineering from the University of Alabama, Huntsville, in 1992.

She has been with Science Systems and Applications, Inc., Hampton, VA, to support the NASA CERES, NEWS, and NPP projects, since December 2006. Previously, she was with Science Applications International Corporation to support CERES project. She has more than ten years of experience in satellite data analysis by working with CERES Clouds Working group to develop surface emissivity maps, cloud analysis, and product software.

David R. Doelling received the B.S. degree in meteorology from the University of Utah, Salt Lake City, in 1985, and the M.S. degree in atmospheric science from the University of Washington, Seattle, in 1991.

Since 1989, he has been with the Science Directorate, NASA Langley Research Center, Hampton, VA, as a Contractor, working with the ERBE science team. He is currently the CERES Time in Space Subsystem Lead responsible for the spatial and temporal averaging of CERES cloud properties and fluxes into level-3 products. He is involved in the calibration of geostationary sensors with MODIS for consistent cloud properties and deriving broadband fluxes from geostationary radiances to incorporate the diurnal signal in CERES cloud and flux products.

David F. Young received the B.S. degree in astrophysics from Michigan State University, East Lansing, in 1977, and the M.S. degree in meteorology from the Pennsylvania State University, University Park, in 1979.

Since 1996, he has been with the National Aeronautics and Space Administration (NASA) Langley Research Center, Hampton, VA, where he currently serves as the Deputy Director of the Science Directorate. His main areas of research include satellite remote sensing of cloud microphysical and radiation parameters and the development of data fusion techniques for the generation of high-accuracy climate data records.

Dr. Young is a member of the CERES Science team and the Leader of the CLARREO Mission Study Team.

Douglas A. Spangenberg received the B.S. and M.S. degrees in meteorology from The Pennsylvania State University, University Park, in 1993 and 1995, respectively.

He has been with the NASA Langley Research Center, Hampton, VA, since 1997, through contracts with Analytical Services and Materials, Inc. and Science Systems and Applications, Inc. His primary work is focused on supporting the CERES project, and he has extensive experience in satellite cloud property retrieval validation. He has developed many algorithms for the display, analysis, and calibration of data from geostationary and polar orbiting satellites using the Man Computer Interactive Data Access System. His research interests include detecting and analyzing polar cloud systems using NOAA-AVHRR, and Terra and Aqua MODIS data.
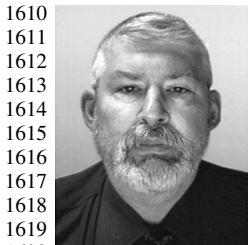
Walter F. Miller received the B.S. degree in meteorology from the University of Lowell, Lowell, MA, in 1979, and the M.S. degree in atmospheric science from Creighton University, Omaha, NE, in 1982.

He is currently a Senior Engineer with Science Systems and Applications, Inc., Hampton, VA, working on the CERES Data Management Team. Previously, he supported the CERES project with the Science Application International Corporation. From 1979 to 1996, he was a Weather Officer with the United States Air Force. His research interest includes data fusion of various satellite-borne remote sensing instruments.
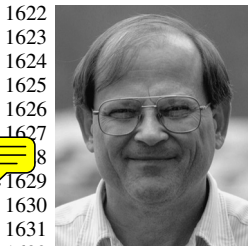
Bruce A. Wielicki received the B.S. degree in applied math and engineering physics from the University of Wisconsin–Madison, Madison, in 1974, and the Ph.D. degree from Scripps Institution of Oceanography, University of California, San Diego, La Jolla, in 1980.

Since 1980, he has been with the Science Directorate, NASA Langley Research Center, Hampton, VA, where he is currently a Principal Investigator on the CERES (Clouds and the Earth's Radiant Energy System) satellite-based observations of the Earth's radiation budget on Terra, Aqua, and NPP (2010) missions. He has also been a Coinvestigator on the Landsat, CloudSat, and CALIPSO satellite missions. His research focuses on the role of clouds, aerosols, and radiation in climate change.

Dr. Wielicki is a fellow of the American Meteorological Society. He received the AMS Henry G. Houghton Award and the NASA Scientific Achievement and Leadership Medals.

Ricky R. Brown received the B.S. degree in business administration and the B.S. degree in computer science from Christopher Newport University (CNU), Newport News, VA, in 1989 and 1998, respectively.

He has been with Science Systems and Applications, Inc., Hampton, VA, supporting the NASA CERES project, since December 2006. He also worked for SAIC supporting NASA CERES projects. He has ten-year experience with the CERES Clouds Working Group and CERES Data Management Team with software development, data analysis, and validation.

Sharon C. Gibson received the B.S. degree from California Polytechnic State University, San Luis Obispo, and the M.S. degree in imaging science from Rochester Institute of Technology.

Early in her career, she focused on remote sensing as applied to the acid rain problem in the Adirondack lakes. She also contributed to algorithms that launched a major document processing system product line, and helped a large photographic film manufacturer "go digital." Since 1992, she has enjoyed supporting atmospheric science research under the NASA CERES, DIAL, and HALOE programs, analyzing field experiment and satellite data and developing analysis and visualization software. She is currently with Science Systems and Applications, Inc., Hampton, VA.

Erika B. Geier received the B.S. and M.S. degrees in computer science from the College of William and Mary, Williamsburg, VA, in 1984 and 1991, respectively.

Since 1994, she has been with the Science Directorate, NASA Langley Research Center, Hampton, VA, supporting the CERES and FLASHFlux projects. Prior to becoming a Civil Servant, she worked as a NASA Contractor and supported the LASE project. She is currently the Data Management Lead for CERES on the Terra, Aqua, and NPP satellites.

AUTHOR QUERIES

AQ1 = Please provide specific address of "Analytical Services and Materials, Inc."
AQ2 = The author's current affiliations were captured from the curriculum vitae. Please check if appropriate.
AQ3 = "VIRS" has two expanded forms: "Visible and Infrared Scanner" and "Visible Infrared Scanner". The latter was followed.
AQ4 = Please check if the list in this sentence is correctly enumerated.
AQ5 = Two occurrences of "Aqua Ed 1a" were changed to "Aqua Ed1a". Please check if appropriate.
AQ6 = Please check if this sentence is correct.
AQ7 = Please provide publication update in Ref. [13].
AQ8 = Please provide publication update in Ref. [14].
AQ9 = Please provide publication update in Ref. [15].
AQ10 = Please provide publication update in Ref. [54].
AQ11 = "Science Directorate" was obtained from the affiliations footnote and inserted here as part of the author's current affiliation. Please check if appropriate.
AQ12 = The author's current affiliation was taken from the first footnote. Please check if appropriate.
AQ13 = "Science Directorate" was obtained from the affiliation footnote and inserted here as part of the author's current affiliation. Please check if appropriate.
AQ14 = "Science Directorate" was obtained from the affiliations footnote and inserted here as part of the author's current affiliation. Please check if appropriate.
AQ15 = Please provide the address of "Rochester Institute of Technology".
AQ16 = The author's current affiliation was taken from the first footnote. Please check if appropriate.

Note: "no. 29" was deleted in Ref. [55]. Please check.
     All occurrences of "sun glint" were changed to "sunglint".

END OF ALL QUERIES